ELSEVIER

Contents lists available at ScienceDirect

Computers and Structures

journal homepage: www.elsevier.com/locate/cas





Coupled FDM-SPH modeling of CFRP-reinforced concrete damage under combined blast and fragment impact

Jian-Yu Chen a, b,*, Jidong Zhao a,**, Ruo-Feng Feng A, Rui-Chen Ni C, Chong Peng D

- ^a Department of Civil and Environmental Engineering, The Hong Kong University of Science and Technology, HKSAR, China
- b School of Safety Science and Engineering, Nanjing University of Science and Technology, 200 Xiaolingwei Street, Xuanwu District, Nanjing, 210094, China
- ^c Zhejiang Geely Holding Group Co., Ltd., Hangzhou, 310000, China
- ^d School of Civil Engineering, Southeast University, 211189, Nanjing, China

HIGHLIGHTS

- A coupled FDM-SPH scheme was proposed to study CFRP-concrete damage under blast loadings.
- The solver uses an orthotropic model to simulate CFRP composites under impact loadings.
- The coupled method was validated by a variety of impact and blast problems.
- The method efficiently captures deformation, crack propagation, and energy absorption in structures.

ARTICLE INFO

Keywords: Carbon fiber reinforced polymer FDM-SPH Reinforced concrete Blast loading Fragments

ABSTRACT

Reinforced concrete (RC) structures reinforced with carbon fiber-reinforced polymer (CFRP) composites are increasingly popular for blast-resistant designs, yet their failure mechanisms under combined blast and fragment loading remain poorly understood due to challenges in modeling multi-physics phenomena such as shockwave propagation, fluid-structure interaction, and fracture dynamics. This study introduces a novel GPU-accelerated finite difference method -smoothed particle hydrodynamics (FDM-SPH) framework to evaluate damage in CFRP-concrete composite structures subjected to extreme loading. The framework couples SPH for structural damage prediction with FDM for air blast simulation, linked via an immersed boundary method to enable bidirectional fluid-structure coupling. The framework is validated against multiple cases, including high-velocity impact on CFRP laminates and close-range blast loading, demonstrating strong agreement with experimental data. Detailed analysis of CFRP-concrete composites reveals that CFRP significantly mitigates blast-induced deformation, reducing displacement by 38 % compared to single CFRP plate while absorbing 73 % of impact energy through delamination and fiber fracture. The model uniquely captures synergistic damage from combined blast and fragment loads, showing localized penetration and global deformation not observed under isolated loading. These findings underscore CFRP's efficacy in enhancing blast resilience and provide a validated computational tool for optimizing composite structures in defense and critical infrastructure applications.

1. Introduction

Reinforced concrete (RC) is widely used in both engineering and military applications due to its cost-effectiveness, high compressive strength, and excellent resistance to blast and impact loads. However, RC structures can experience severe damage when subjected to close-in blast loading. To improve their resilience, novel reinforcement materials-such

as carbon fiber reinforced polymers (CFRP) and polyurea coatings-have been introduced as external retrofitting solutions. Among these, CFRP has gained particular attention owing to its outstanding durability, high strength-to-weight ratio, and stiffness. CFRP is a composite material composed of carbon fibers embedded within a polymer matrix, which serves to bind the fibers and transfer loads. Its superior mechanical performance under extreme conditions has led to widespread application

Email addresses: chenjianyu@njust.edu.cn (J.-Y. Chen), jzhao@ust.hk (J. Zhao).

^{*} Corresponding author at: Department of Civil and Environmental Engineering, The Hong Kong University of Science and Technology, HKSAR, China.

^{**} Corresponding author

across various industries, including aerospace, shipbuilding, automotive, and civil engineering. Given its advantageous properties, it is essential to investigate the dynamic response of CFRP-reinforced concrete structures under blast loading. A comprehensive understanding of this interaction is crucial for optimizing CFRP use in enhancing the blast resistance and overall structural performance of RC systems subjected to extreme loading scenarios.

Several researchers have conducted analytical and experimental studies to investigate the damage mechanisms of composite structures subjected to blast loading. For example, Puente et al. [1] developed an analytical model for high velocity impacts on thin CFRPs woven laminated plates based on an energy balance. Wang et al. [2] examined the behavior of square reinforced concrete (RC) slabs under blast loads and analyzed their damage modes and mechanisms across varying blast intensities. They also proposed damage criteria corresponding to different levels of structural damage. Yan et al. [3] explored the performance of CFRP-strengthened RC columns subjected to close-in blast loading through a combination of experimental tests and finite element simulations. Their results demonstrate that CFRP significantly enhances the blast resistance of RC columns. Similarly, Reifarth et al. [4] studied CFRP-reinforced concrete specimens exposed to blasts at varying distances and charge weights, showing that CFRP can significantly improve the resilience of critical infrastructure against blast effects. Despite their value, blast experiments are inherently costly, time-consuming, and dangerous. Moreover, they face limitations in capturing the complex multi-phase and multi-physics phenomena associated with blast scenarios, such as fluid-structure interaction, shock wave propagation, material interface motion, and fracture propagation in reinforced concrete at micro time scales. Experimental results are also constrained to specific test configurations and cannot be easily extrapolated to different blast scenarios or geometrical scales.

As a result, mesh-based numerical methods, such as finite element (FE) analysis, are commonly employed to simulate the dynamic response of composite structures under blast loading. For instance, Anas et al. [5-7] employed a Coupled Eulerian-Lagrangian (CEL) formulation within the finite element framework of ABAQUS to examine the response of singly reinforced one-way concrete slabs subjected to concentric contact blast loading. Similarly, Rajput et al. [8,9] analyzed the behavior of glass fiber-reinforced polymer (GFRP) reinforced concrete (RC) tunnels under internal blast loading using an explicit three-dimensional finite element (FE) approach. Studies by Kumar et al. [10] and Maazoun et al. [11] used finite element simulations to model RC slabs subjected to blast loads, successfully reproducing phenomena such as spalling, scabbing, and crater formation. However, mesh-based methods encounter difficulties in accurately modeling large deformations, as they are prone to issues such as mesh distortion, mass loss, negative densities, and negative volumes-especially under high-strain-rate events like explosions-often leading to numerical instability or failure. In contrast, meshless methods such as the discrete element method (DEM) [12], peridynamics [13], and smoothed particle hydrodynamics (SPH) [14] have emerged as promising alternatives. These methods can more robustly capture the progressive damage and failure of target structures subjected to blast and impact loading, including complex interactions like sand-blast coupling effects.

In the present research, the smoothed particle hydrodynamics (SPH) method is employed to predict the structural response of reinforced concrete (RC) under blast loading. The Lagrangian particle-based SPH methodology, originally proposed by Monaghan [15] and Lucy [16], is well-suited for modeling the dynamic behavior of solid materials subjected to high-strain-rate phenomena such as impact and explosions. Owing to its Lagrangian nature, SPH can effectively capture large deformations and material failure in solid structures under extreme loading conditions. For example, Feng et al. [17] introduced a density-adaptive SPH technique to address large density ratios in explosive welding simulations. Their work demonstrated the method's capability to accurately reproduce critical physical phenomena such as shock wave propagation,

jet formation, flyer plate acceleration, and welding interface morphology. Chen et al. developed SPH solvers for a variety of complex explosive scenarios, including three-dimensional soil explosions [18], underwater explosions [19], and shaped charge penetration into ceramic-steel composite targets [20]. The numerical results from these studies showed good agreement with available experimental data. Furthermore, Sun et al. [21] proposed an adaptive SPH volume scheme for modeling strongly compressible multiphase flows involving large volume changes, such as cavitation bubble dynamics, and validated it through several challenging benchmark tests. Recent studies have also explored hybrid techniques. Shi et al. [22] and Yang et al. [23] developed coupled peridynamics-SPH (PD-SPH) models to investigate quasi-brittle fracture in ice subjected to high-velocity water jet impacts, and to simulate interactive thermo-mechanical responses and thermal fracturing in solid materials

However, while SPH excels in modeling solid deformation, it faces limitations in accurately capturing shock wave propagation in compressible air. In contrast, finite difference methods (FDM) are preferred for modeling shock waves in air due to their superior accuracy and computational efficiency. Therefore, a coupled FDM-SPH framework is proposed in this study to simulate the entire physical process of blast interaction with CFRP-reinforced composite structures. In this framework, the finite difference method is used to model shock wave propagation in air, while the SPH method captures the large deformation and damage evolution in solid materials. To handle the interaction between the fluid (air) and solid domains, the immersed boundary method (IBM) proposed by Peskin [24] is incorporated. IBM facilitates the transfer of physical variables across the FDM-SPH interface, enabling seamless coupling of the two solvers. Furthermore, to enhance computational efficiency, the CUDA parallel computing platform [25] is adopted, leveraging the power of thousands of GPU cores to significantly accelerate the FDM-SPH computations.

This paper is organized as follows: Section 2 introduces the proposed FDM-SPH solver, detailing the fundamentals of SPH and FDM, as well as the implementation of the immersed boundary method. Section 3 presents numerical case studies, including the damage assessment of CFRP laminate plates under high-velocity impact, and the response of RC and CFRP-RC composite structures subjected to closerange blast loading, simulated using the proposed FDM-SPH solver. Section 4 summarizes the main novelties, findings, and conclusions of the research.

2. Numerical method

In this physical phenomenon, the expansion of explosive gaseous products and its induced shock wave propagation cause deformation in the surrounding structures. The dynamic response of solid structures subjected to blast loading and fragments, as well as the motion of compressible fluids, is governed by the Navier-Stokes (N-S) equations [26],

$$\begin{cases} \frac{d\rho}{dt} = -\rho \nabla \cdot \boldsymbol{v}, \\ \frac{d\boldsymbol{v}}{dt} = \frac{1}{\rho} \nabla \cdot \boldsymbol{\sigma} + \boldsymbol{b}, \\ \frac{d\boldsymbol{e}}{dt} = \frac{1}{\rho} \boldsymbol{\sigma} : (\nabla \otimes \boldsymbol{v}). \end{cases}$$
(1)

in which, ρ is the density; \boldsymbol{v} is the velocity; e is the internal energy; σ is the stress tensor; \boldsymbol{b} is the external force. For the solid material, the stress component in σ is normally calculated via constitutive models. The explosive detonation can be treated as inviscid and adiabatic process, and consequently the stress component of the fluid domain depends on an equation of state. Hence a constitutive relation for obtaining the stress tensor can be defined by,

$$\sigma = \begin{cases} -pI, & x \in \Omega^f; \\ -pI + S, & x \in \Omega^s. \end{cases}$$
 (2)

where p and I are hydrostatic pressure and unit matrix, respectively; S is the deviatoric stress tensor; Ω^f and Ω^s denote the fluid domain and solid domain, respectively.

2.1. SPH description of solid structures

2.1.1. Basic idea of the SPH method

In the coupled FDM-SPH solver, the SPH method is employed to predict the dynamic behavior of CFRP-reinforced concrete materials, due to its natural ability to capture large deformations and material fragmentation. The SPH formulation consists of two main steps: kernel approximation and particle approximation. In the kernel approximation, a physical variable associated with particle i is expressed using a smoothing kernel function W. In practice, these kernel functions approach the Dirac delta function as the smoothing length h tends to zero, ensuring consistency of the approximation. In the particle approximation, the physical variable associated with particle i is further approximated by the summation of the neighboring particles. The SPH approximations of the value of a field function f(x) and its gradient $\nabla f(x)$ are given by,

$$\langle f(\mathbf{x}) \rangle \cong \sum_{i=1}^{N} \frac{m_j}{\rho_j} f(\mathbf{x}_j) W\left(\mathbf{x} - \mathbf{x}_j, h\right);$$
 (3)

$$\langle \nabla f(\mathbf{x}) \rangle \cong -\sum_{j=1}^{N} \frac{m_j}{\rho_j} f(\mathbf{x}_j) \nabla W\left(\mathbf{x} - \mathbf{x}_j, h\right).$$
 (4)

The Wendland function that can prevent particles clumping and penetration is used as the kernel function in SPH [27],

$$W(q,h) = \alpha_d \begin{cases} \left(1 - \frac{q}{2}\right)^4 (2q+1) & 0 \le q < 2; \\ 0 & q \ge 2. \end{cases}$$
 (5)

where the normalization constant $\alpha_d = 7/(4\pi h^2)$ in two dimensions and $\alpha_d = 21/(16\pi h^3)$ in three dimensions; $q = \frac{|\mathbf{x}|}{h}$ is the normalized distance. The smoothing length h_i associated with particle i is updated using the following equation [28],

$$\frac{dh_i}{dt} = -\frac{1}{d} \frac{h_i}{\rho_i} \frac{d\rho_i}{dt}.$$
 (6)

With the use of standard SPH divergence and gradient operator, the discretized form of the governing equation expressed in Eq. (1) can be determined in the following,

$$\begin{cases} \frac{\mathrm{d}\rho}{\mathrm{d}t} = \sum_{j=1}^{N} m_{j} \left(\boldsymbol{v}_{i} - \boldsymbol{v}_{j} \right) \cdot \nabla_{i} W_{ij} & (a) \\ \frac{\mathrm{d}\boldsymbol{v}_{i}}{\mathrm{d}t} = \sum_{j=1}^{N} m_{j} \left(\frac{\boldsymbol{\sigma}_{i} + \boldsymbol{\sigma}_{j}}{\rho_{i}\rho_{j}} + \Pi_{ij} \boldsymbol{I} \right) \cdot \nabla_{i} W_{ij} & (b) \\ \frac{\mathrm{d}\boldsymbol{e}_{i}}{\mathrm{d}t} = \frac{1}{2} \sum_{j=1}^{N} m_{j} \frac{p_{i} + p_{j}}{\rho_{i}\rho_{j}} \left(\boldsymbol{v}_{i} - \boldsymbol{v}_{j} \right) \cdot \nabla_{i} W_{ij} + \frac{1}{2\rho_{i}} \boldsymbol{S}_{i} \boldsymbol{\varepsilon}_{i} & (c) \\ p_{i} = p(\rho_{i}, \boldsymbol{e}_{i}) & (d) \end{cases}$$

where ρ_i , w_i , v_i , e_i and p_i are the density, mass, velocity, energy, and pressure of particle i, respectively; Π_{ij} is artificial viscosity; σ is stress tensor; S is deviatoric stress tensor; ϵ is the strain rate tensor. The artifical viscosity proposed by Monaghan [15] that can reduce numerical oscillations is introduced in the discretized equation.

$$\Pi_{ij} = \begin{cases}
\frac{-\alpha c_{ij} \phi_{ij} + \beta \phi_{ij}^2}{\rho_{ij}} & \mathbf{v}_{ij} \cdot \mathbf{x}_{ij} < 0; \\
0 & \mathbf{v}_{ij} \cdot \mathbf{x}_{ij} \ge 0.
\end{cases}$$
(8)

Here, $\phi_{ij}=\frac{h_{ij}v_{ij}\cdot x_{ij}}{|x_{ij}|^2+(\varphi)^2}$, $c_{ij}=\frac{1}{2}(c_i+c_j)$, $\rho_{ij}=\frac{1}{2}(\rho_i+\rho_j)$, $h_{ij}=\frac{1}{2}(h_i+h_j)$, $v_{ij}=v_i-v_j$, and $x_{ij}=x_i-x_j$. $\alpha=2.0$ and $\beta=10.0$ are adopted to stabilize the numerical scheme and avoid excessive artificial dissipation.

The tensile instability, which leads to unphysical particle clustering, is a well-known issue in SPH. Over the past two decades, the artificial pressure/stress method has been the primary approach to address it. More recently, new strategies have been proposed: Rabczuk et al. [29] introduced updated Lagrangian kernel formulations for simulating the dynamic response of solids, while Zhang et al. [30] developed a generalized non-hourglass updated Lagrangian formulation that improves structural response predictions. In this study, we adopt the artificial pressure method [31], which provides stable results in our numerical tests.

$$T_{ij} = f_{ii}^n \left(R_i + R_j \right), \tag{9}$$

where $f_{ij} = W_{ij}/W(\Delta x)$ and Δx is the initial particle spacing; the exponential factor n is taken as $n = W(0)/W(\Delta x)$; the term R_i is calculated using

$$R_{i} = \begin{cases} \frac{\varepsilon |p_{i}|}{\rho_{i}^{2}} & \text{if } p_{i} < 0; \\ 0 & \text{otherwise.} \end{cases}$$
 (10)

 ε is a constant parameter controlling the artificial stress, which is usually taken as 0.2 [31].

A fixed boundary condition was applied in all numerical cases, with all velocity components constrained to zero along the plate boundaries.

2.1.2. The constitutive model and failure model for CFRP

CFRP is an orthotropic, brittle, and non-pressure-sensitive material whose mechanical behavior is strongly influenced by fiber orientation and ply stacking sequence-markedly different from the isotropic and quasi-brittle characteristics of concrete. In the present study, carbon fiber-reinforced polymer (CFRP) is modeled as a homogeneous orthotropic material to simplify its complex layered structure. The mechanical response is governed by an orthotropic constitutive model, which defines the stress-strain relationship along the principal material directions.

$$\sigma = C\varepsilon$$
 (11)

where σ is the stress tensor; ϵ is the strain tensor; C is the stiffness tensor. If the tensors are described in terms of the components, then

$$\sigma_{ij} = C_{ijkl} \varepsilon_{kl} \tag{12}$$

The stiffness matrix of a homogeneous orthotropic material can be written as

$$\begin{pmatrix} \dot{\sigma}_{11} \\ \dot{\sigma}_{22} \\ \dot{\sigma}_{33} \\ \dot{\sigma}_{23} \\ \dot{\sigma}_{13} \\ \dot{\sigma}_{12} \end{pmatrix} = \begin{pmatrix} \frac{1}{E_1} & \frac{-\nu_{21}}{E_2} & \frac{-\nu_{21}}{E_3} & 0 & 0 & 0 \\ \frac{-\nu_{12}}{E_1} & \frac{1}{E_2} & \frac{-\nu_{23}}{E_3} & 0 & 0 & 0 \\ \frac{-\nu_{13}}{E_1} & \frac{-\nu_{23}}{E_2} & \frac{1}{E_3} & 0 & 0 & 0 \\ 0 & 0 & 0 & \frac{1}{G_{23}} & 0 & 0 \\ 0 & 0 & 0 & 0 & \frac{1}{G_{13}} & 0 \\ 0 & 0 & 0 & 0 & 0 & \frac{1}{G_{13}} \end{pmatrix} \begin{pmatrix} \dot{\epsilon}_{11} \\ \dot{\epsilon}_{22} \\ \dot{\epsilon}_{33} \\ \dot{\epsilon}_{23} \\ \dot{\epsilon}_{13} \\ \dot{\epsilon}_{12} \end{pmatrix}$$

$$(13)$$

where E_i is the Young's modulus; G_{ij} is the shear modulus; v_{ij} is the Poisson's ratio. The principle axes of the fiber reinforced composite are denoted in Fig. 1, in which the x direction denotes the direction of the fiber, y and z denote the directions perpendicular to the fiber.

The progressive damage model [32] and quadratic delamination criterion proposed by Brewer [33] are implemented in the in-house SPH code to predict the failure behavior of CFRP.

1) Fiber breakage

$$\left(\frac{\sigma_{11}}{X_T}\right)^2 + \left(\frac{\sigma_{12}}{S_{12}}\right)^2 \ge 1\tag{14}$$

where X_T is longitudinal tensile strength in each ply; S_{12} is the in-situ ply shear strength. When the combined stresses σ_{11} and σ_{12} satisfy the criterion, this layer fails by either fiber breakage or fiber matrix shearing.

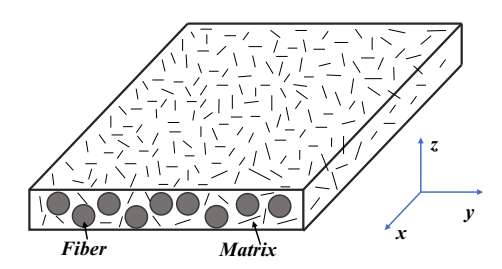


Fig. 1. The schematic diagram of the fiber reinforced composite, where the x direction denoted the direction of the fiber, y and z denote the directions perpendicular to the fiber.

2) Matrix cracking

$$\left(\frac{\sigma_{22}}{Y_T}\right)^2 + \left(\frac{\sigma_{12}}{S_{12}}\right)^2 \ge 1\tag{15}$$

where Y_T is the transverse tensile strength. This criterion states that when the stresses σ_{22} and σ_{12} satisfy the above equation, matrix cracking occurs in that layer.

3) Matrix crushing

$$\left(\frac{1}{4}\frac{\sigma_{22}}{Y_T}\right)^2 + \frac{Y_C\sigma_{22}}{4S_{12}} + \frac{\sigma_{22}}{Y_C} + \left(\frac{\sigma_{12}}{S_{12}}\right)^2 \ge 1 \tag{16}$$

where Y_T is the compressive strength in the transverse direction.

4) Delamination

$$\left(\frac{\sigma_{33}}{Z_T}\right)^2 + \left(\frac{\sigma_{23}}{S_{23}}\right)^2 + \left(\frac{\sigma_{13}}{S_{13}}\right)^2 \ge 1 \tag{17}$$

where Z_T is the tensile strength in the thickness direction. σ_{23} and σ_{13} are shear stresses.

2.2. FDM for compressible flows

The hyperbolic form of Eq. (1) is adopted for describing the physical process of the shock wave propagation in the compressible air medium. Neglecting effects of viscosity and heat conductivity, the Eq. (1) is rewritten as the conservative 3-D Euler equation according to,

$$\frac{\partial \mathbf{U}}{\partial t} + \frac{\partial \mathbf{F}_1}{\partial x} + \frac{\partial \mathbf{F}_2}{\partial y} + \frac{\partial \mathbf{F}_3}{\partial z} = \boldsymbol{\phi}$$
 (18)

The vectors of conservative variables U, F_1 , F_2 , F_3 are listed in the following.

$$U = \begin{pmatrix} \rho \\ \rho u \\ \rho v \\ \rho w \\ \rho E \end{pmatrix}, F_1 = \begin{pmatrix} \rho u \\ \rho u^2 + p \\ \rho u v \\ \rho u w \\ (\rho E + p) u \end{pmatrix}, F_2 = \begin{pmatrix} \rho v \\ \rho u v \\ \rho v^2 + p \\ \rho v w \\ (\rho E + p) v \end{pmatrix}, F_3 = \begin{pmatrix} \rho w \\ \rho u w \\ \rho v w \\ \rho w^2 + p \\ (\rho E + p) w \end{pmatrix}$$
(19)

where ρ is the fluid density; u, v, and w are velocities in x, y, and z directions; p is pressure; E is the specific internal energy. The source terms ϕ include body forces and external forces such as gravity. The ideal gas equation of state $p = (\gamma - 1) \rho \left[E - \frac{1}{2} \left(u^2 + v^2 + w^2 \right) \right]$ is used to close the governing equation, where γ is the ratio of specific heats. The explicit third-order Runge-Kutta method which is used for the numerical solution of the ordinary differential equation takes the form,

$$\begin{cases} U^{(1)} = (I + \Delta t \mathcal{L}) U^n; \\ U^{(2)} = 3/4 U^n + 1/4 (I + \Delta t \mathcal{L}) U^{(1)}; \\ U^{n+1} = 1/3 U^n + 2/3 (I + \Delta t \mathcal{L}) U^{(2)}. \end{cases}$$
(20)

where operator $\mathcal{L} = \mathcal{L}_x + \mathcal{L}_y + \mathcal{L}_z$; \mathcal{L}_x , \mathcal{L}_y , and \mathcal{L}_z represent the spatial operators in x, y, and z directions. \mathcal{I} is the identity matrix. The flux

derivative associated with node i with respect to x dimension is obtained as

$$\frac{\partial F}{\partial x}\Big|_{i} = \frac{1}{\Delta x} \left[\hat{F}_{i+\frac{1}{2}} - \hat{F}_{i-\frac{1}{2}} \right],\tag{21}$$

where F is the convective flux vector. $\hat{F}_{i+\frac{1}{2}}$ is a numerical flux, which typically is a Lipschitz continuous function of values of several neighboring nodes.

$$f(u) = f^{+}(u) + f^{-}(u), \tag{22}$$

where f is a scalar flux. $f^+(u)$ corresponds to the sub-flux associated with the positive derivative of f with respective to u, i.e. $\frac{df^-(u)}{du} \geq 0$; $f^-(u)$ corresponds to the negative derivative, i.e. $\frac{df^-(u)}{du} \leq 0$.

$$\hat{f}_{i+\frac{1}{2}}^{+} = \sum_{n=0}^{N} \omega_n^+ q_n^+ (f_{i+n-N}^+, \dots, f_{i+n}^+), \tag{23}$$

where

$$q_0^+(f_{i-1}^+, \dots, f_i^+) = (-f_{i-1}^+ + 3f_i^+)/2;$$

$$q_1^+(f_i^+, \dots, f_{i+1}^+) = (f_i^+ + f_{i+1}^+)/2;$$

$$\omega_n^+ = \frac{\alpha_n^+}{\alpha_0^+ + \dots + \alpha_N^+},$$
(24)

where N=r-1=1; r is the number of candidate stencils. Based on each stencil $S_n=(x_{i+n-N},\ldots,x_{i+n})$, we obtain q_n , which are the r-th order approximations of $\hat{f}_{i+1/2}$; ω_n are actual weights of q_n ; α_n^+ can be determined as

$$\alpha_n^+ = \frac{C_n}{(\varepsilon + LS_+^+)^2},\tag{25}$$

where $\varepsilon=10^{-6}$; IS_n^+ $(IS_1^+=(f_i^+-f_{i-1}^+)^2$ and $IS_2^+=(f_{i+1}^+-f_i^+)^2)$ indicates the smoothness of solution on S_n ; $C_0=1/3$ and $C_1=2/3$.

2.3. Immersed boundary method for shock-structure interaction

The immersed boundary method (IBM) is incorporated into the developed solver to facilitate the exchange of physical information between fluid grid nodes and solid SPH particles. Specifically, interface quantities are obtained by interpolating surrounding Eulerian grid/SPH values onto Lagrangian markers with a weighting function; the force on the solid is computed from the local momentum balance and applied to the structure, while the equal and opposite reaction is conservatively spread back to the fluid to ensure momentum conservation. As illustrated in Fig. 2, the first step in treating the fluid-solid interface is to classify the computational domain into three distinct regions: the fluid region, the solid region, and the fluid-structure interface.

Once the regions are identified, the physical variables at the interface nodes are computed by interpolating values from neighboring SPH particles. For example, the velocity at a fluid–structure interface node is obtained by interpolating the velocities of SPH particles located within the cell that contains the node.

$$\mathbf{v}_{c}^{ib} = \sum_{i=1}^{N} \frac{1}{N} \mathbf{v}_{i}. \tag{26}$$

Correspondingly, according to the conservation of momentum, the external force imposed on SPH particles can be determined based on the numerical flux increments,

$$f_{i}^{k} = -\frac{\left(\Delta\left(\rho v\right)\right)_{c}^{k} - v_{c}^{ib}(\Delta\rho)_{c}^{k}}{\Delta t} = \alpha^{k} \left(v_{c}^{ib} RHS_{c}^{k}\left(\rho\right) - RHS_{c}^{k}\left(\rho v\right)\right)$$
 (27)

in which $\mathrm{RHS}^k_c(\rho)$ and $\mathrm{RHS}^k_c(\rho\nu)$ are increments of the mass and momentum caused by surface fluxes, respectively. $\alpha^k \in \left(1,\frac{1}{4},\frac{2}{3}\right)$ is the coefficient of the third-order Runge-Kutta method.

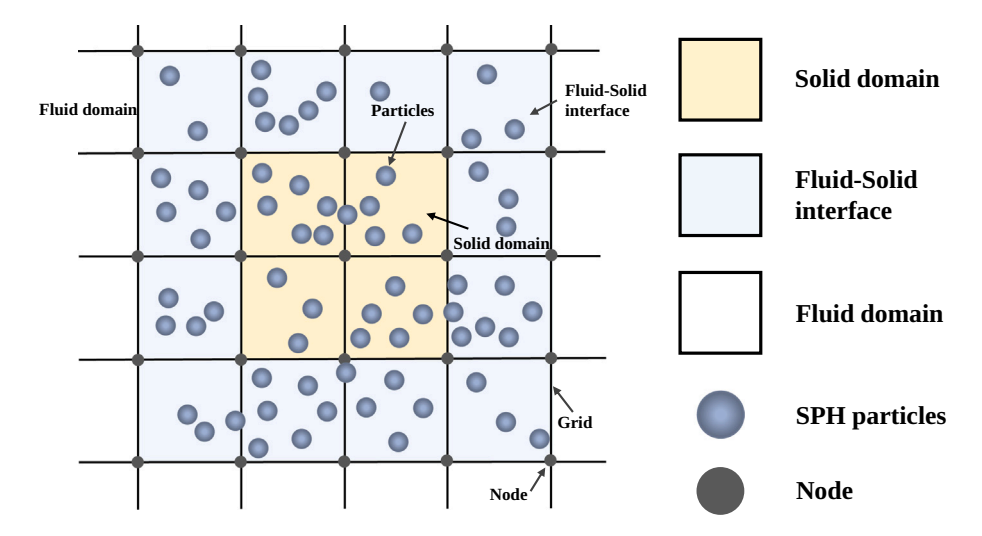


Fig. 2. Classification of three different regions, namely the fluid region, solid region, and fluid-structure interface.

The reaction force is evenly distributed among SPH particles,

$$F_i^k = \frac{1}{n_c} f_i^k V_c. \tag{28}$$

 n_c is the number of particles in cell c; V_c is the volume of cell c.

$$F_i = \frac{1}{6}F_i^1 + \frac{2}{3}F_i^2 + F_i^3. \tag{29}$$

Other physical variables such as the density, energy can be interpolated using the neighboring nodes.

$$\psi_I = \frac{\sum w(d_N)\psi_N}{\sum w(d_N)}.$$
(30)

where ψ_N is physical variable at node N; $w(d_N)$ is the weight function; d_N is the distance between two different nodes.

2.4. Solution procedure of the FDM-SPH method

The coupled FDM-SPH method is employed to solve strong fluid-structure interaction problems. The overall solution procedure is outlined as follows. Initially, all data related to SPH particles and finite difference (FD) nodes are stored in CPU memory. After initialization, the data are transferred to GPU memory for high-performance computation. All core computational steps involving SPH and FDM are executed on the GPU to maximize efficiency.

The first step on the GPU is the classification of the computational domain into three distinct regions: the fluid region, the solid region, and the fluid-structure interface. The fluid region is solved using the finite difference method (FDM), while the solid region is handled by the smoothed particle hydrodynamics (SPH) method. The fluid-structure interface is treated using the immersed boundary method (IBM), which couples the FDM and SPH solvers to accurately model interactions between fluids and solids. In the fluid domain, the Steger-Warming flux splitting scheme which ensures numerical stability and accurate capturing of shocks and discontinuities is employed to maintain the upwinding nature of the scalar fluxes, and a third-order Runge-Kutta method is used for time integration of the physical variables. Once these variables are updated, the external forces acting on SPH particles are computed from the increments in density and momentum fluxes. The dynamic response of solid structures is then predicted using the SPH formulation. Finally, the numerical results obtained from the coupled FDM-SPH solver are transferred from GPU back to CPU for storage and post-processing. Additional details on the prediction of solid structural behavior and fluid motion are presented in Algorithm 1.

Algorithm 1: Solution procedure of the GPU-accelerated FDM-SPH solver for one computational time step.

- Classify the computational domain into three regions: fluid domain, solid domain, and fluid-structure interface.
- Apply physical boundary conditions and treat the immersed boundary. Determine the velocity of interface nodes based on neighboring SPH particles (see Eq. 26); compute density and energy using interpolation from surrounding fluid nodes (see Eq. 30).
- 3. Perform flux splitting using the Steger-Warming scheme.
- Calculate numerical fluxes using the third-order WENO scheme (see Eq. 23).
- 5. Update physical variables of the fluid nodes using the third-order Runge-Kutta method (see Eq. 20).
- Compute the external force acting on SPH particles using Eqs. (27) and (29).
- 7. Update the solid domain using the SPH method. Calculate the elastic trial deviatoric stress $S_i^{\alpha\beta}$ (see Eq. A.12).
- Check whether the material response is elastic or plastic using the yield criterion (see Eq. A.15).
- Determine the final deviatoric stress using the classical radial return algorithm.
- 10. Compute the incremental plastic strain.
- 11. Update the damage coefficient *D* for the concrete material (see Eq. A.3).
- 12. Compute the pressure *p* using the appropriate constitutive model (see Eqs. A.17, and A.5–A.9).
- 13. Repeat from Step 1 for the next time step.

3. Numerical results and discussion

In the following sections, two numerical cases are presented to validate the proposed FDM-SPH solver: (1) a three-dimensional high-velocity impact of an aluminum sphere on a CFRP laminate plate, and (2) damage assessment of a CFRP laminate plate subjected to close-range blast loading. Since the concrete HJC constitutive model has already been validated in our previous work [20], the focus here is on validating the accuracy of the CFRP constitutive model and the FDM-SPH coupling strategy. Subsequently, the developed FDM-SPH solver is applied to investigate the damage mechanisms, failure patterns, and affected areas of CFRP-reinforced concrete composite structures under close-range blast

loading, as well as under combined blast and fragment impact scenarios. All simulations were performed on a single NVIDIA GeForce RTX 4090 GPU. The parallel computational performance and accuracy of the proposed FDM-SPH method have been thoroughly evaluated in our prior study [34] through a series of fluid-structure interaction benchmarks.

3.1. Validation examples

3.1.1. High velocity impact of CFRP laminate plate

In order to validate the implementation of the constitutive model of the CFRP laminate implemented in the SPH solver, the high velocity impact of a metal sphere on a CFRP laminate plate was conducted. The initial configuration of the high velocity impact of the CFRP laminate plate is shown in Fig. 3. The velocity magnitude of this aluminum sphere is 4,960 m s⁻¹, and the diameter of the sphere is 1.5 mm. The dimensions of the CFRP plate are 30 mm \times 30 mm \times 2.3 mm. This CFRP composite structure consists of sixteen plies with the laminate lay-ups [+45/0/ – 45/90]. The initial particle spacing is 0.075 mm, and a total of 4,780,097 particles are involved in this simulation. All of the sides of the CFRP laminate plate are fixed. The parameters for CFRP composite structure taken as the typical values by Ref. [35] are summarized in

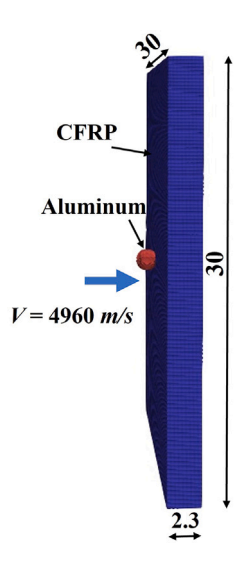


Fig. 3. Initial configuration of the high velocity imapet of Aluminum sphere on the CFRP laminate plate. All of the dimensions are in mm.

Table 1Parameters of the CFRP constitutive model [35].

E ¹¹ (GPa) 150	E ²² (GPa) 8.2	E ³³ (GPa) 8.2	E ²³ (GPa) 2.7	E ¹³ (GPa) 4.34	E ¹² (GPa) 4.34
v ²³ 0.53	v ²³ 0.34	v ²³ 0.34	X ^T (MPa) 2700	<i>Y</i> ^T (MPa) 63.7	Z^T (MPa) 63.7
$Y^{C}(MPa)$ 235	Z ^C (MPa) 235	S ²³ (MPa) 112	S ¹³ (MPa) 140	S ¹² (MPa) 140	

Table 2Johnson-Cook model parameters of the aluminum medium [36].

A (MPa)	B (MPa)	C	n	k	T _{room} (K)	T _{melt} (K)
265	426	0.015	0.34	1.0	502	0.0

Table 3Parameters used for the Mie-Grüneisen EOS for aluminum [36].

ρ_0 (kg m ⁻³)	C_0 (km s ⁻¹)	S_1	S_2	S_3	γ	α	E_0 (J)
2768	5240	1.4	0	0	1.97	0.48	0

Table 1. The parameters of the Mie–Grüneisen EOS and the Johnson-Cook constitutive model referenced from Ref. [36] for the prediction of the dynamic behavior of the aluminum sphere are summarized in Tables 2 and 3, respectively.

The temporal evolution of the velocity distribution of the CFRP composite structure subjected to the high velocity impact of the aluminum sphere at different times 5 μs , 10 μs , 15 μs , 20 μs , and 25 μs is depicted in Fig. 4. After the aluminum sphere impacts the CFRP plate, the sphere initially deforms elastically, causing stress concentration at the point of impact. Since the velocity of the sphere is high enough, some of the kinetic energy of the sphere is partly transferred to the kinetic energy of the CFRP plate, plastic deformation occurs in the sphere and the CFRP materials (4 (a-b)). The impact of the aluminum sphere caused localized deformation of CFRP, such as denting and crushing (4)(c)–(d). As shown in Fig. 11, it can be observed that the matrix cracks, and fibres get fractured and delaminated due to the high stress at the contact point. As the stress waves propagate, they may lead to the separation of individual layers of the CFRP composite structure. Furthermore, the numerical profile of the debris cloud and the damage pattern (delamination and fracture) are compared with the available experimental radiograph from Ref. [37], and it can be found that the damage pattern of the CFRP plate is in general agreement with the experimental data. More specifically, as shown in Table 4, the numerical perforation diameter of the CFRP plate subjected to the high velocity impact is close to the experimental data, the relative error between the experimental and numerical data is less than 10 %. The convergence of the perforation diameter in the CFRP composite structure is presented in Fig. 6. As the SPH particle spacing decreases, the perforation diameter gradually converges to approximately 6.2 mm.

The temporal evolution of the energy distribution of the entire dynamic system has also been studied. The temporal evolution of the total energy, kinetic energy, and internal energy of the high velocity impact of CFRP is depicted in Fig. 7. Upon impact, a portion of the kinetic energy of the aluminum sphere is transferred to the internal energy and the kinetic energy of the CFRP plate. Consequently, the total kinetic energy decreases from 60 J to 10 J gradually. The plastic deformation and the delamination and cracking of the CFRP plate contribute to the kinetic energy loss. Afterwards, the total energy, kinetic energy, and the internal energy reach a steady state and maintain constant values. Note that the total energy of the dynamic system is nearly a constant value 60 J, which shows the conservation of the energy. Additionally, the temporal evolution of the energy of the single CFRP plate is shown in Fig. 8. Since the portion of the kinetic energy of the aluminum sphere is transmitted to the energy of the CFRP plate, it can be observed that the all of the kinetic energy, internal energy, and the total energy of the CFRP structure increase to 9 J, 42 J, and 51 J, respectively. Nearly 73 % (Portion = Internal energy of the CFRP / Total energy of the system) of the total energy of the explosive detonation is absorbed by the CFRP plate during the impact process. Overall, the numerical results including the damage pattern, perforation diameter, and the energy evolution obtained from the GPU-accelerated SPH model indicate that the developed SPH solver is capable of capturing the damage and delamination of CFRP structure very well (Fig. 5).

3.1.2. Damage assessment of CFRP laminate plate subjected to close-range blast loading

In this numerical test, a Carbon-Polyester laminate plate subjected to close-range blast loading was simulated using the developed FDM-SPH solver to validate the accuracy of the FDM-SPH coupling strategy and the computation of external forces acting on SPH particles. The initial configuration of the CFRP laminate plate under blast loading is illustrated in Fig. 9. The computational domain measures 0.27 m \times 0.27 m \times 0.442 m. A 100 g spherical plastic explosive (equivalent to 168 g of TNT) is positioned above the laminate plate, suspended 0.4 m from its top surface. The CFRP laminate plate consists of seven plain-woven fabric plies stacked in a [0/90] configuration, with all warp fibers aligned in the

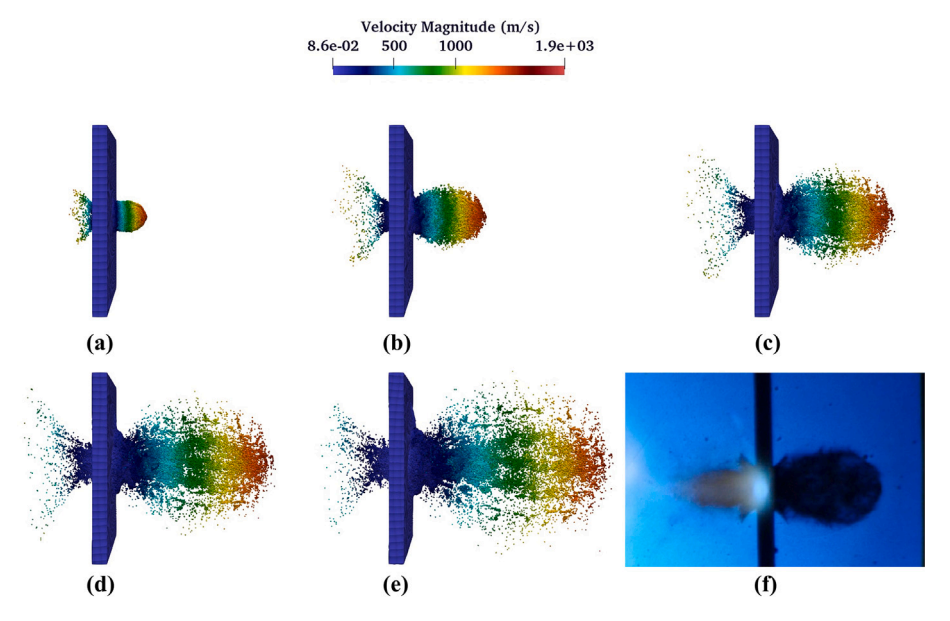


Fig. 4. Temporal evolution of the velocity distribution of the high velocity impact on CFRP composite structure at different times 5 μs , 10 μs , 15 μs , 20 μs , and 25 μs and experimental data obtained form [37] at 14 μs .

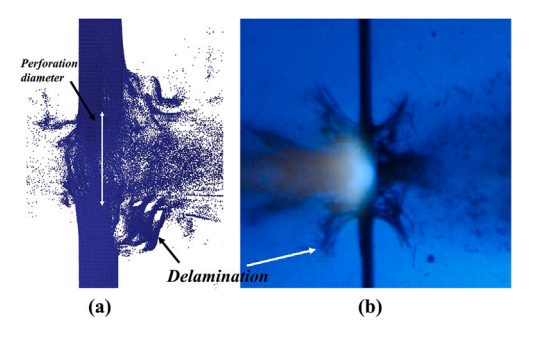


Fig. 5. Numerical delamination of the CFRP composite structure subjected to high velocity impact of Aluminum sphere at 25 μs and experimental damage profile of CFRP structure from Ref. [37].

Table 4A comparison of the numerical results for the CFRP obtained from the FVM-SPH solver with those measured experimentally by Ref. [37].

Damage (mm)	Computation	Experiment	Discrepancy (%)
Perforation diameter	6.20	5.98	3.6

same direction. The plate dimensions are 0.25 m \times 0.25 m \times 0.0042 m, resulting in an individual ply thickness of 0.6 mm. The initial particle resolution is set to 0.0003 m, yielding a total of 9,020,557 SPH particles. The initial mesh size for the fluid domain is 0.0012 m. Material properties for the CFRP are adopted from Ref. [38], and summarized in Table 5. For the fluid domain, all boundaries are modeled with outlet flow conditions. The boundaries of the CFRP laminate plate are fully fixed to simulate clamped constraints on all sides.

The temporal evolution of pressure distribution during shockwave propagation in the air medium and the CFRP laminate plate, as computed by the developed FDM-SPH solver, is shown in Fig. 10 at selected time instances: 0.02 ms, 0.05 ms, 0.1 ms, 0.15 ms, 0.2 ms, 0.3 ms, and 0.49 ms. Following detonation, a three-dimensional spherical shock wave is generated and propagates through the surrounding air. At

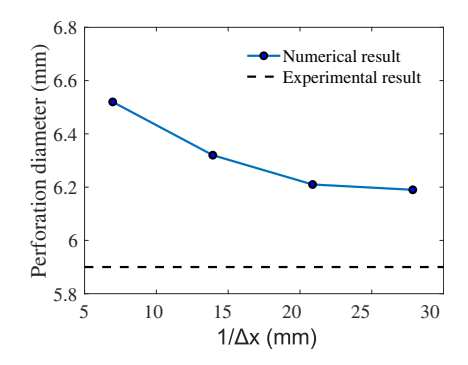


Fig. 6. Perforation diameter of the CFRP plate subjected to HVI.

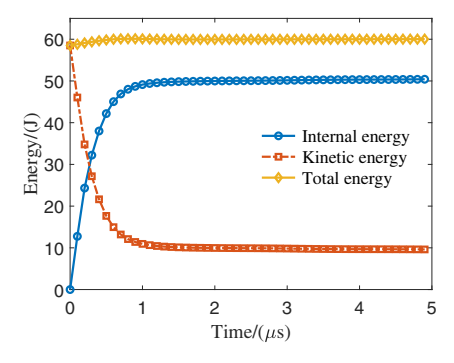


Fig. 7. Temporal evolution of the energy of the CFRP composite structures subjected to high velocity imapct.

approximately 0.12 ms, the shock wave reaches the top surface of the CFRP plate and subsequently interacts with the structure. Upon impact, the shock wave transmits into the CFRP material, where both reflection and refraction phenomena are observed, as clearly illustrated in Fig. 10. As shown in Fig. 11, the numerical blast-induced delamination cracking is in general agreement with the experimental X-ray computed

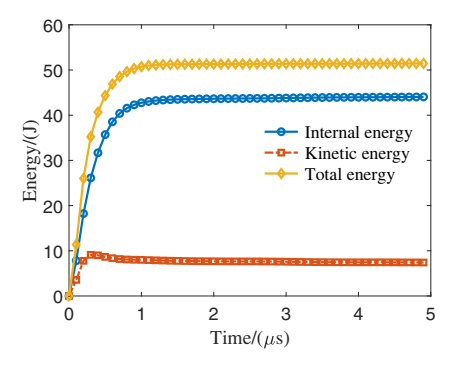


Fig. 8. Temporal evolution of the energy of the CFRP composite structures subjected to high velocity imapct.

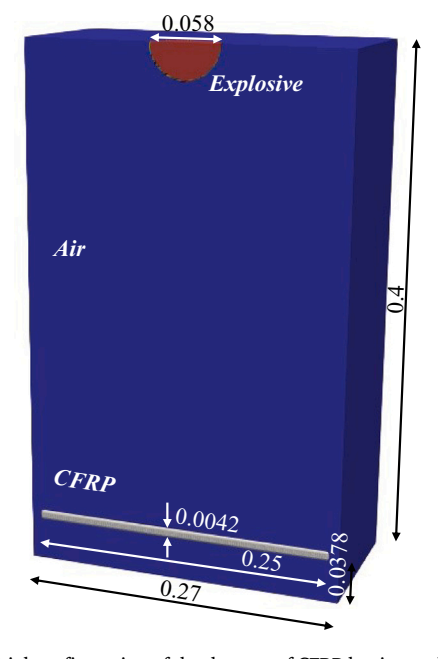


Fig. 9. The initial configuration of the damage of CFRP laminate plate subjected to close-range blast loading. All of the dimensions are in m.

Table 5Parameters of the CFRP constitutive model [38].

E ¹¹ (GPa) 55	E ²² (GPa) 55	E ³³ (GPa) 7.0	E ²³ (GPa) 4.5	E ¹³ (GPa) 1.8	E ¹² (GPa) 1.8
v^{23} 0.25	v^{23} 0.25	v^{23} 0.25	X^T (MPa) 680	Y^T (MPa) 680	Z^T (MPa) 680
$Y^C(MPa)$ 240	Z ^C (MPa) 240	S ²³ (MPa) 112	S ¹³ (MPa) 140	S ¹² (MPa) 140	

tomography cross-sectional image [38]. The time history of pressure at a representative point A (located on the top surface of the CFRP plate) is presented in Fig. 12. The pressure at point A rises sharply to a peak of approximately 6.2 MPa, then gradually decays to around 0.18 MPa. The simulated displacement of the CFRP laminate at the central point between 0.15 ms and 0.35 ms shows overall agreement with experimental data reported in [38]. The observed discrepancies between the numerical and experimental results can likely be attributed to two main factors. First, the deformation of CFRP structures under blast loading is highly sensitive to local material variations, manufacturing defects, and boundary conditions-factors that are challenging to fully replicate in numerical simulations. Second, experimental blast loading introduces

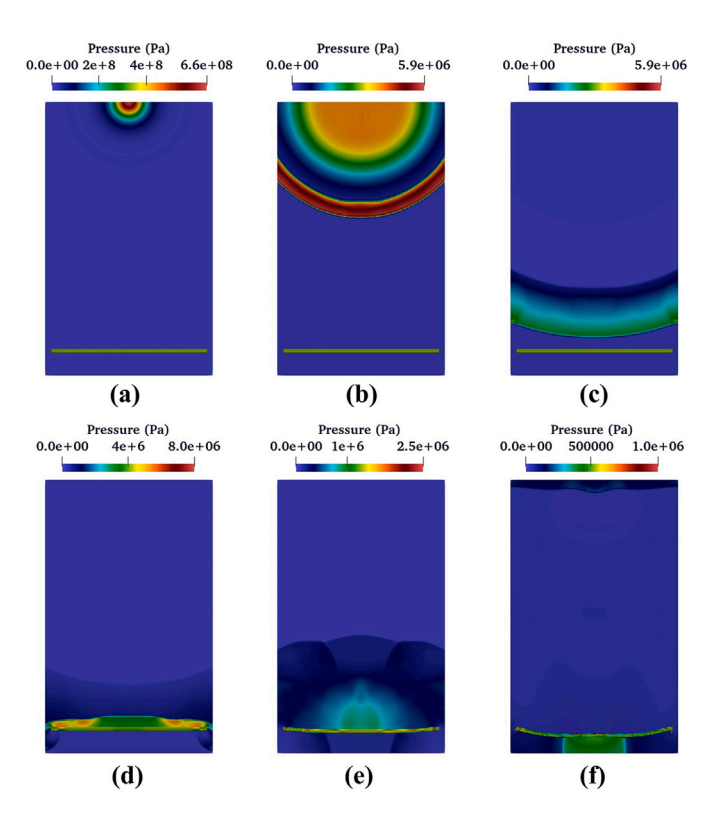


Fig. 10. Temporal evolution of the pressure distribution of the damage of CFRP plate subjected to blast loading at different times 0.02 ms, 0.05 ms, 0.1 ms, 0.15 ms, 0.2 ms, 0.3 ms, and 0.49 ms.

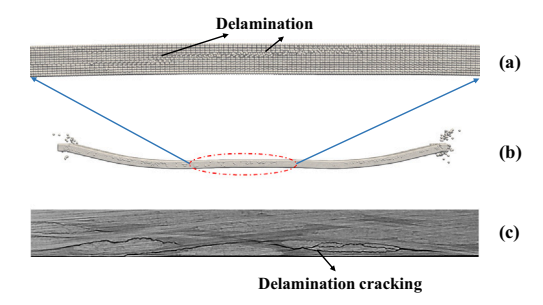


Fig. 11. Comparison of the numerical blast-induced delamination cracking (ab) and the experimental X-ray computed tomography cross-sectional image [38] (c).

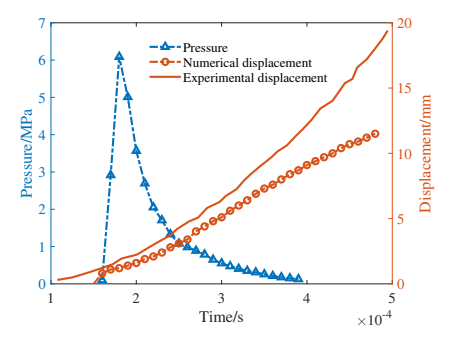


Fig. 12. Temporal evolution of the pressure at the typical point of the fluid domain and the numerical and experimental [38] displacement of the center point of the CFRP composite structure.

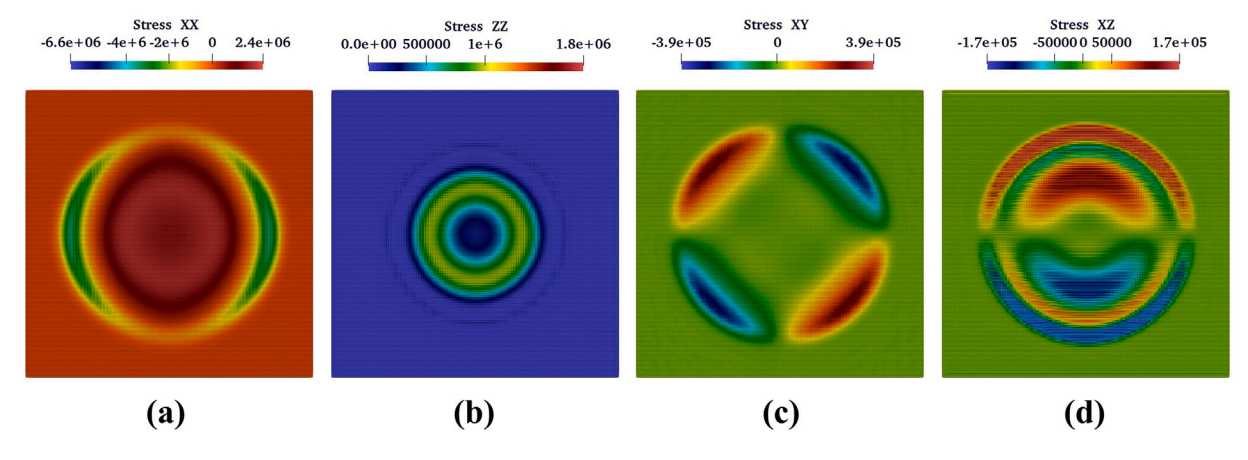


Fig. 13. The components of the stress tensor distribution of the CFRP plate subjected to blast laoding at 0.17 ms.

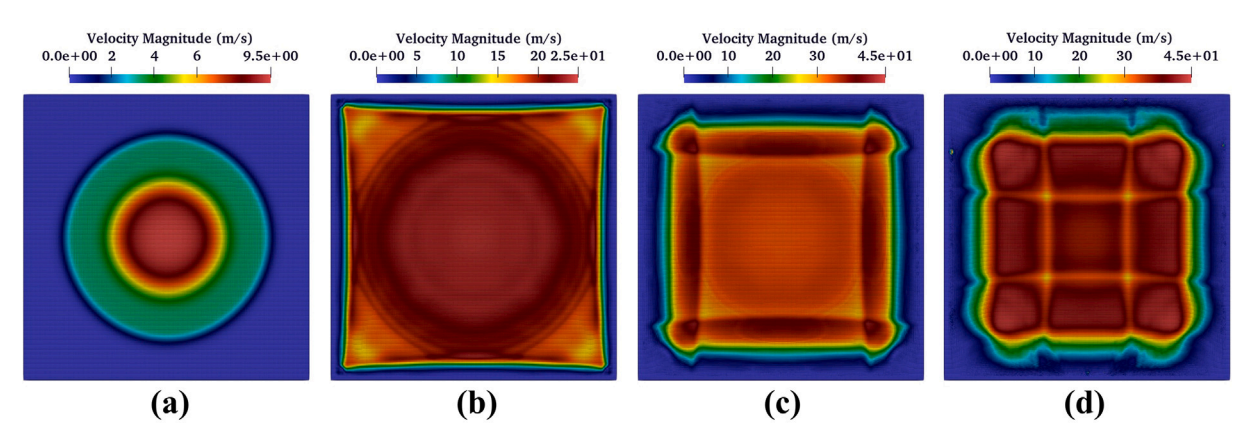


Fig. 14. Temporal evolution of the velocity distribution of the damage of CFRP plate subjected to blast laoding at different times 0.17 ms, 0.2 ms, 0.25 ms, and 0.30 ms.

inherent variability due to inconsistencies in charge placement, ignition, and pressure wave propagation, which contribute to scatter in the measured structural response.

The components of the stress tensor distribution of the CFRP plate in the X direction σ_{xx} subjected to blast loading at 0.17 ms are shown in Fig. 13. It can be found that the stress σ_{xx} is symmetric with respect to the Y axis. The stress tensor components of the CFRP plate σ_{xy} is symmetric with respect to the line x=y, and the largest value of the stress σ_{xy} is 0.39 MPa. Overall, the stress distribution within the CFRP structure is smooth and free from significant fluctuations or numerical noise.

Additionally, the temporal evolution of the velocity distribution of the CFRP composite plate at different time instances-0.17 ms, 0.2 ms, 0.25 ms, and 0.30 ms-is illustrated in Fig. 14. It is observed that the velocity at a representative point on the plate rapidly increases to approximately 45 m/s at 0.25 ms, followed by a gradual decline due to plastic deformation of the material. The temporal evolution of the displacement of the CFRP composite structure is shown in Fig. 12. The displacement progressively increases, reaching a peak of approximately 10.2 mm at 0.42 ms, as a result of the shock wave impact. Furthermore, the damage pattern predicted by the proposed FDM-SPH solver is compared with experimental observations reported by Ref. [39]. The comparison indicates that the developed solver accurately captures both the deformation and damage characteristics of the CFRP plate subjected to close-range blast loading, thereby validating its effectiveness for modeling high-fidelity fluid-structure interaction problems.

3.2. Application examples

3.2.1. Damage assessment of CFRP-concrete structures subjected to close-range blast loading

As demonstrated in the previous section, the single CFRP structure exhibits high strength and lightweight characteristics; however, it is susceptible to deformation under blast loading due to its relatively low compressive strength. Integrating a concrete medium can significantly enhance the overall load-bearing capacity and improve the structure's resistance to impact and blast loads. Therefore, this study investigates the damage performance of composite structures by employing a CFRP-concrete system that combines carbon fiber reinforced polymer (CFRP) with concrete.

Building on the validation of the CFRP constitutive model and the FDM-SPH coupling implemented in the developed FDM-SPH solver, this section further explores the damage assessment of CFRP-concrete composite structures subjected to close-range blast loading. The analysis begins with an examination of the damage mechanisms of CFRP-concrete composites under blast impact, followed by a comparative study of the damage characteristics across different CFRP-concrete configurations.

The initial setup of the CFRP-concrete structure under blast loading is illustrated in Fig. 15. The computational domain measures $1.2~\mathrm{m} \times 1.2~\mathrm{m} \times 0.6~\mathrm{m}$. The specimen consists of a reinforced concrete slab bonded to a CFRP plate. The CFRP slab is firmly glued to the bottom surface of the concrete slab, ensuring a strong bond between the two materials. Blast loading is induced by a 0.2 kg cylindrical TNT explosive placed 0.4 m

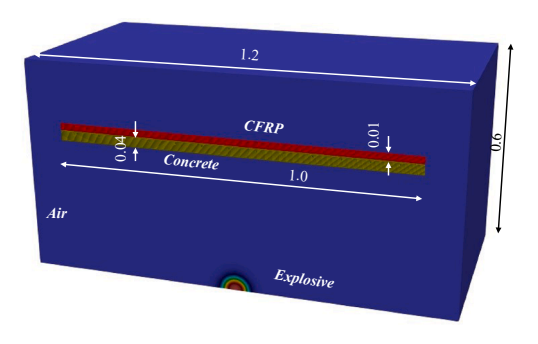


Fig. 15. Initial configuration of the damage of the concrete-CFRP composite structure subjected to blast loading.

below the slab. The reinforced concrete slab dimensions are $1000~\text{mm} \times 1000~\text{mm} \times 40~\text{mm}$ (length \times width \times thickness). Reinforcement consists of 6 mm diameter steel bars arranged in two layers of longitudinal and transversal bars, with a spacing of 75 mm between adjacent bars.

As summarized in Table 6, numerical simulations were conducted for four different composite structure configurations: a single concrete plate, a single CFRP plate, and two CFRP-reinforced concrete plates. The total thickness of the combined plates in each case is identical. The particle spacing is set to 2 mm, resulting in a total of 5,976,024 particles involved across all simulations. The mesh size is fixed at 6 mm. For the material modeling, the HJC constitutive model and the Johnson-Cook constitutive model, detailed in the Appendix, are employed to predict the dynamic behavior of concrete and steel, respectively. The HJC model is widely adopted for concrete under dynamic loading due to its ability to capture strain rate sensitivity, damage evolution, and pressure dependence. Similarly, the Johnson-Cook model effectively describes the behavior of isotropic ductile metals subjected to high strain rates and temperatures. The parameters for the CFRP composite, Johnson-Cook steel model, and Grüneisen equation of state (EOS) are listed in Tables 5, 7, and 8, respectively. In all numerical cases, the boundaries of the composite structure (SPH particles) are fixed, while all boundaries of the fluid domain are treated as outflow conditions.

Firstly, we studied the three-dimensional damage of the CFRP-reinforced concrete plate under blast loading (scenario 2). The physical process of the damage of the CFRP-concrete composite structure subjected to blast loading at different times 0.10 ms, 0.12 ms, 0.15 ms, 0.18 ms, 0.20 ms, and 0.25 ms is depicted in Fig. 16. After the ignition of the

Table 6
Different combinations of the concrete and
CFRP composite structures. All of the dimensions are in mm.

Scenario	1	2	3	4
CFRP	44.0	6.0	4.0	0.0
Concrete	0	38.0	40.0	44.0

Table 7Johnson-Cook model parameters of steel [36].

A (MPa)	B (MPa)	C	n	k	T_{room} (K)	T _{melt} (K)
792	510	0.014	0.26	1.03	273	1793

 Table 8

 Parameters used for the Mie-Grüneisen EOS for steel [40].

$\rho_0 ({\rm kg} \; {\rm m}^{-3})$	$C_0 \text{ (km s}^{-1}\text{)}$	S_1	S_2	S_3	γ	α	E ₀ (J)
7830	4.569	1.49	0	0	2.17	0.46	0

explosive, the shockwave propagates in the air medium. The shockwave impacts the bottom surface of the composite structure at $0.11\,\mathrm{ms}$. Then the shockwave is reflected and refracted from the plate.

The temporal evolution of the velocity distributions of the CFRP and reinforced concrete plate at different times-0.20 ms, 0.25 ms, 0.30 ms, and 0.50 ms-is shown in Fig. 17. It can be observed that, as part of the shockwave's internal energy is converted into the kinetic energy of the composite structure, the velocity magnitude rapidly increases to 9.8 ms⁻¹, then gradually decreases. The stress distribution of the CFRP plate subjected to blast loading at 0.20 ms is illustrated in Fig. 18. For instance, the shear stress component σ_{xy} exhibits symmetry with respect to the line x=y, while the normal stress component σ_{xx} is symmetric about the *y*-axis. Some short-range noise and minor fluctuations are present in the stress distribution, likely caused by the interactions at the interface between the two different materials, CFRP and concrete.

Subsequently, we compared the displacement at typical points, damage patterns, and energy absorption of the CFRP-reinforced double-layered plate with those of other numerical cases under single blast loading. Fig. 19 illustrates the temporal evolution of the central displacement of the CFRP structure under scenario 3. Following the impact of the shockwave on the bottom surface of the composite plate, the displacement at the center point progressively increases, reaching approximately 5 mm at 1.2 ms. Table 9 presents the displacement of the composite plate's center point. It is evident that the displacement at the center of the single CFRP plate, measuring 7.4 mm, is larger than in the other scenarios, indicating that the single CFRP structure is more susceptible to deformation compared to the composite configurations.

The damage mode and damage area vary noticeably across different scenarios. For instance, in scenario 2, approximately 14 fractures propagate radially within the concrete due to its relatively smaller thickness compared to the other cases. It is also observed that the number of fractures on the top surface of the reinforced concrete decreases from 14 to 6 as the overall thickness of the composite structure increases. Additionally, more circumferential fractures appear on the bottom surface, as shown in Fig. 20.

The energy absorption characteristics of different composite materials are compared in Fig. 21. As shown, the kinetic energy of the single CFRP plate (scenario 1) rapidly increases to approximately 450 J before gradually decreasing to around 70 J. In scenario 2, the kinetic energy of the reinforced concrete-CFRP plate rises to about 350 J at around 400 μs and then stabilizes. Consequently, the single CFRP plate absorbs more kinetic energy than the other scenarios. Moreover, the kinetic energy of the composite structures tends to increase as the proportion of CFRP material decreases. It is also evident that the CFRP-concrete composite in scenario 2 absorbs more internal energy from the shock wave than the single concrete plate. Additionally, the deformation of the CFRPconcrete composite structure is smaller than that of the single CFRP plate. These results suggest that the combined plate in scenario 2 offers a more balanced performance-achieving both effective energy absorption and limited deformation-making it more suitable for military defense applications compared to the other composite structures.

3.2.2. Damage assessment of the composite structures subjected to combined actions of blast and fragments

As demonstrated in previous sections, under single blast loading, the damage mode of the ceramic-CFRP target is primarily material failure caused by structural deformation. In this section, simulations of reinforced concrete-CFRP composite structures subjected to combined blast and fragment impacts are conducted using the developed FDM-SPH method. High-velocity fragment impacts typically cause localized damage and penetration of the target plate, while blast loading leads to widespread structural deformation. The combination of these effects may produce enhanced destructive consequences. Based on the impact performance analysis of composite structures in the previous section, the reinforced concrete-CFRP composite structure from scenario 2 is selected for further study under combined blast and fragment loading.

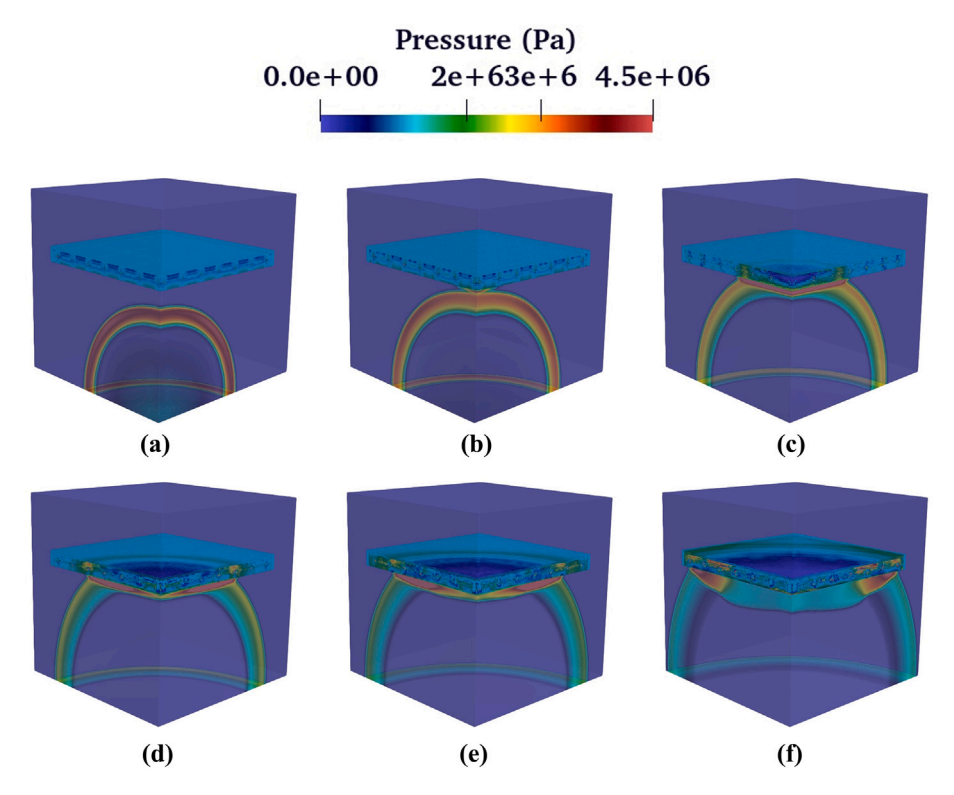


Fig. 16. Physical process of the damage of the CFRP-concrete composite structure subjected to blast laoding at different times 0.10 ms, 0.12 ms, 0.15 ms, 0.18 ms, 0.20 ms, and 0.25 ms.

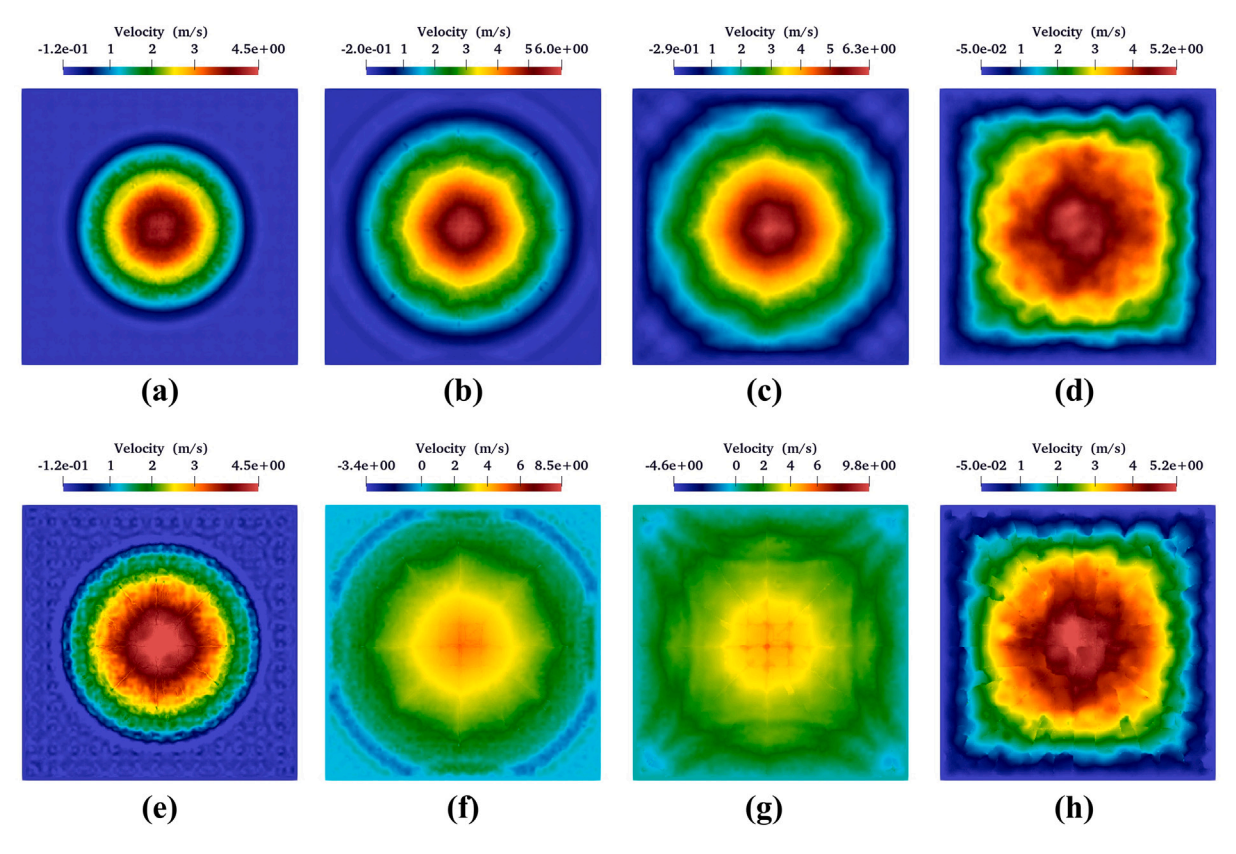


Fig. 17. Temporal evolution of the velocity distribution of the CFRP plate subjected to blast laoding at different times 0.20 ms, 0.25 ms, 0.30 ms, and 0.50 ms.

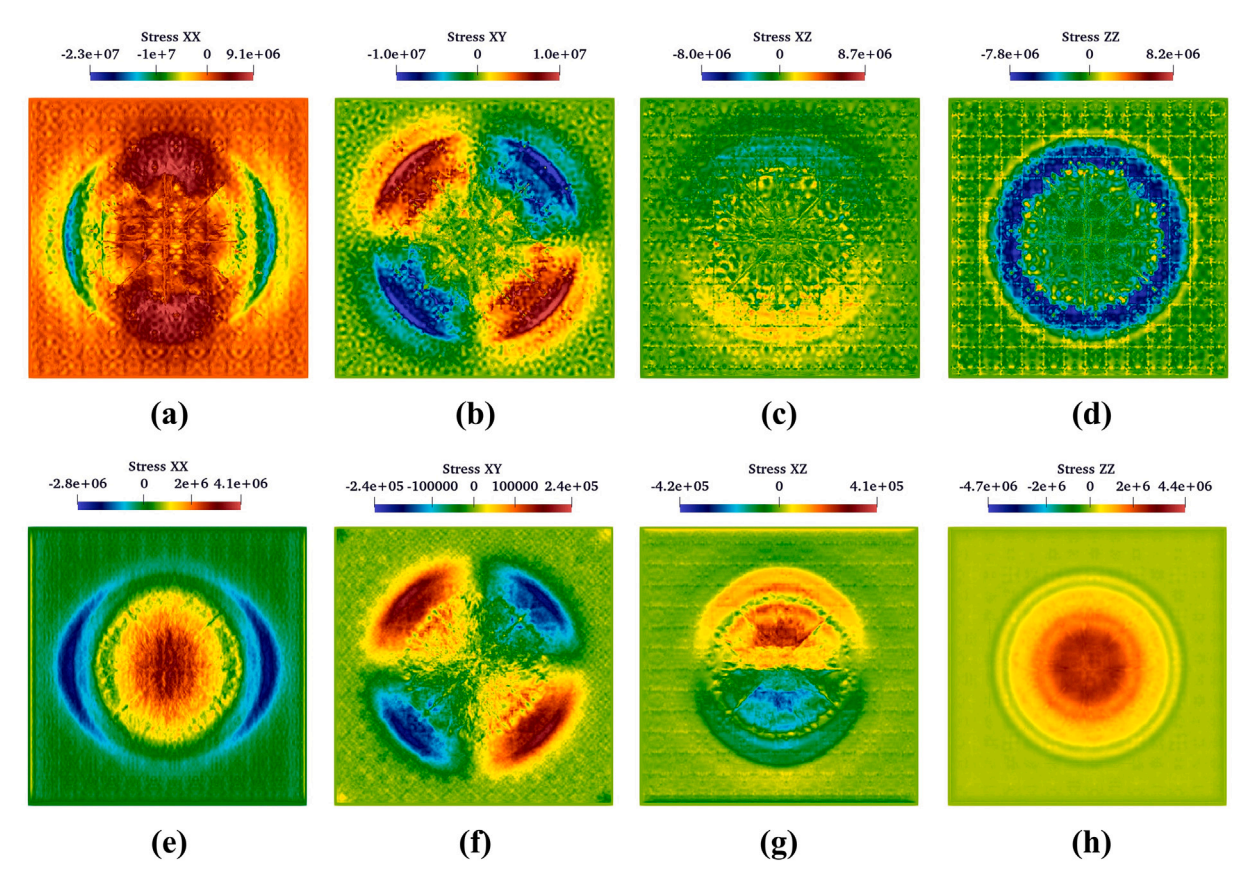


Fig. 18. The stress distribution of the CFRP plate subjected to blast laoding at time 0.20 ms.

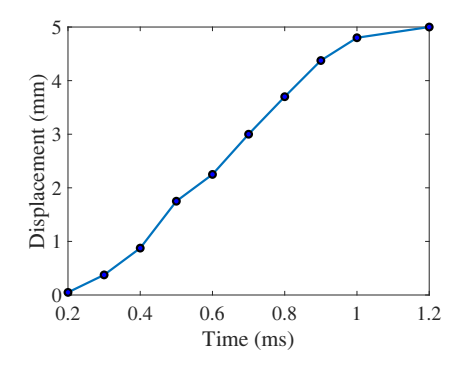


Fig. 19. Temporal evolution of the displacement of the CFRP structure at the center point.

Table 9The displacement at the center point of the different combinations of the concrete and CFRP composite structures at 1.2 ms.

Scenario	1	2	3	4
Displacement (mm)	7.4	5.6	5	2.1

The initial geometry of the composite structure subjected to these combined effects is shown in Fig. 22. This setup is identical to the previous configuration, except that five spherical fragments are introduced above the composite plate's top surface. Each fragment has a diameter of 0.02 m and is positioned 0.22 m away from the explosive charge. The initial particle spacing is 0.006 m, resulting in a

total of 5,747,786 particles in the simulation. The initial mesh size for the computational fluid domain is 0.0002 m. The parameters for the Johnson-Cook constitutive model, Mie-Grüneisen EOS for steel, and the CFRP constitutive model are summarized in Tables 5, 7, and 8, respectively. All boundaries of the composite structure are fixed, while the computational fluid domain employs non-reflecting boundary conditions.

The physical process of the blast loading simulated by the developed FDM-SPH solver at different times-0.02 ms, 0.1 ms, 0.14 ms, 0.2 ms, 1 ms, and 1.62 ms-is shown in Fig. 23. After the explosive ignition, the shock wave propagates through the air medium. The fragments begin to accelerate rapidly due to the shock wave compression. Since the pressure force acting on the central fragment is greater than on the others, its velocity magnitude is higher. The shock wave reaches and impacts the composite structure at approximately 0.42 ms, causing rapid deformation of the CFRP composite. Subsequently, the fragments strike the composite structure around 0.6 ms, leading to delamination of the CFRP plate.

The temporal evolution of the velocity of the typical point of the fragment is shown in Fig. 24. After the ignition of the explosive, all of the fragments are driven by the compression of the shock wave. The velocity of the fragment increases rapidly to 460 ms⁻¹ at 0.18 ms, and then the velocity reaches a steady state. After the fragment impacts the reinforced concrete-CFRP composite structure at around 0.42 ms, since part of the kinetic energy of the fragments is transferred to the kinetic energy of the composite structure, the velocity of the fragment decreases gradually to 220 ms⁻¹ at 1 ms. Finally, the fragment keeps a constant velocity (around 220 ms⁻¹) after penetrating through the reinforced concrete-CFRP composite structure.

The velocity distribution of the spherical fragments, concrete, and CFRP specimen within the composite material at 1.62 ms is shown in

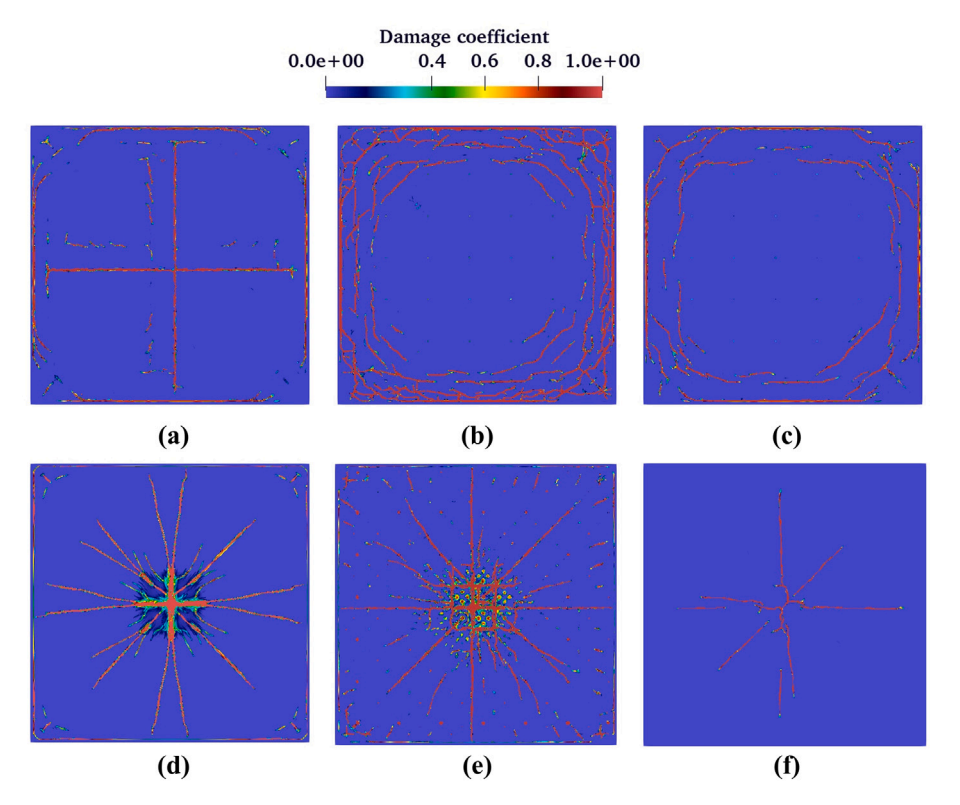
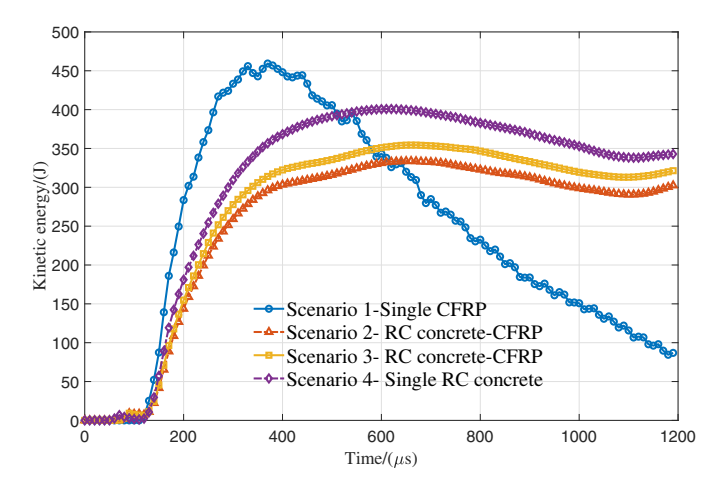


Fig. 20. The damage distributions of the concrete plate subjected to blast loading for scenario 2 (a and d), scenario 3 (b and e), and scenario 4 (c and f) at time 0.35 ms.



 $\textbf{Fig. 21.} \ \ \textbf{Temporal evolution of the kinetic energy of the composite structures} \\ \ \ \textbf{for the different scenarios.}$

Fig. 25. Since the fragments' velocities are higher than that of the CFRP plate, all fragments penetrate through the CFRP layer. Additionally, the damage to the composite structure under the combined blast and fragment loading is compared with the damage observed under blast loading alone in the previous section. Compared to single blast loading, the damage pattern under combined loading is more complex and severe. While blast loading primarily causes large deformation concentrated in the central area, combined loading results in a combination of global structural deformation, interlayer delamination, and significant localized damage due to fragment penetration (see Fig. 25). The localized damage from fragment impact is markedly more severe than that caused by blast loading alone.

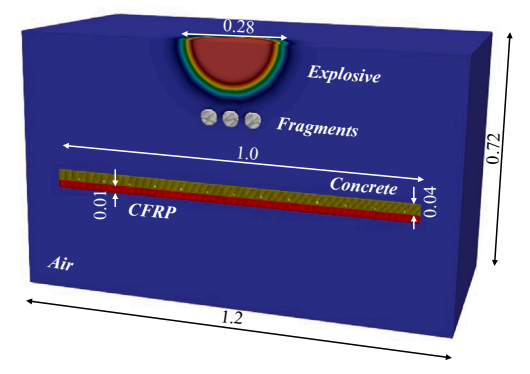


Fig. 22. Initial configuration of the damage of the concrete-CFRP composite structure subjected to blast loading and fragments. All of the dimensions are in m.

4. Discussion and conclusions

In this paper, a coupled FDM-SPH methodology is proposed to study the full process of damage to CFRP-reinforced concrete composite structures under blast loading. The immersed boundary method is employed to couple the deformations of the CFRP-reinforced concrete composite structures with the compressible fluid flow. Firstly, the CFRP constitutive model is validated using high-velocity impact simulations of the CFRP plate. It is found that CFRP layers delaminate and crack under impact loading. Subsequently, the damage to a single CFRP laminate plate subjected to close-range blast loading is simulated to validate the correctness of the coupling of FDM and the SPH method. The displacement of the CFRP material at the center point is in general agreement with the experimental data. Following the validation of the proposed FDM-SPH solver and constitutive models, the damage assessment of

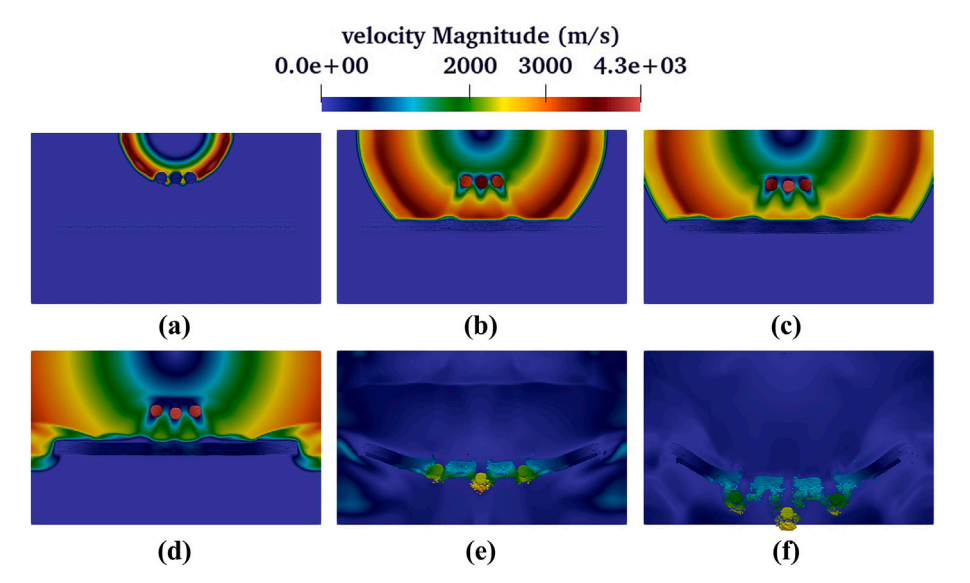


Fig. 23. Temporal evolution of the velocity distribution of the damage of concrete-CFRP composite structures subjected to combined blast loading and fragments at different times 0.02 ms, 0.1 ms, 0.14 ms, 0.2 ms, 1 ms, and 1.62 ms.

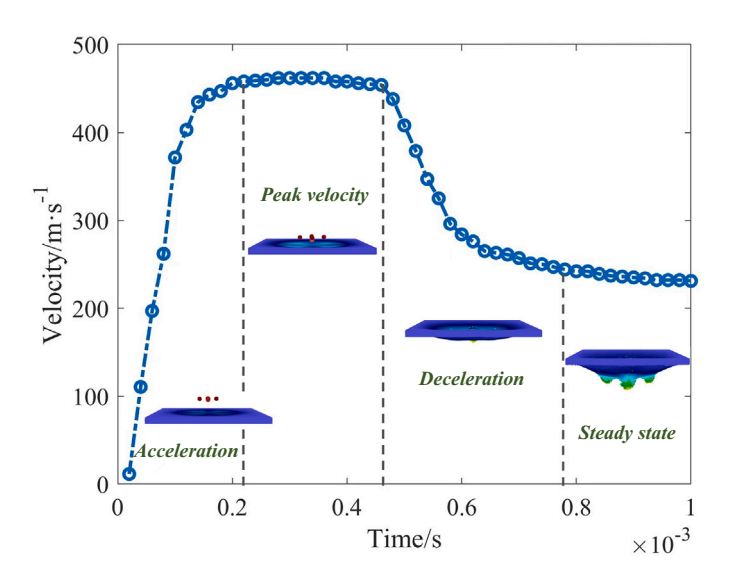


Fig. 24. Temporal evolution of the velocity of the center fragment.

the CFRP-reinforced concrete composite structures subjected to closerange blast loading and combined actions of the fragments and shock wave is conducted. The numerical damage patterns and affected areas obtained from the FDM-SPH model are compared with available experimental data. The main conclusions and novelties of this research are summarized as follows:

(1) Numerical results in 3.2.1 obtained from the FDM-SPH method reveal that CFRP reinforcement fundamentally alters the failure mode of the composite system. While plain concrete exhibits radial, circumferential, and spall fracture patterns consistent with quasi-brittle materials, the addition of CFRP shifts the failure landscape toward fiber-dominated tensile rupture and delamination. Additionally, the CFRP reinforcement increases the absorption of the internal energy of the blast wave through delamination and fracture.

(2) Three dynamic regimes of the temporal evolution of fragment velocity can be classified as follows: rapid acceleration due to blast-driven shock compression; momentum transfer and deceleration upon impact with the composite target; and terminal penetration with steady

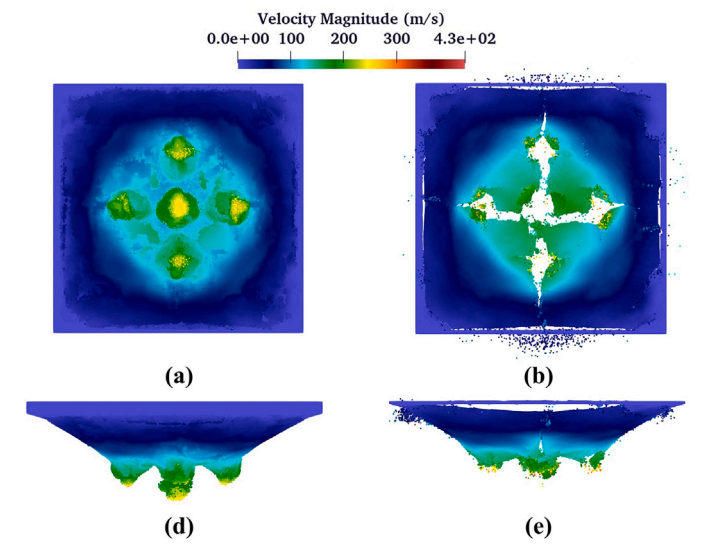


Fig. 25. Temporal evolution of the velocity distribution of the damage of concrete medium (a and d) and CFRP medium (b and e) in the composite structures subjected to combined blast loading and fragments at 1.62 ms.

residual velocity (Fig. 24). The initial spike and subsequent plateau in fragment velocity also imply that most kinetic energy transfer occurs over a narrow timescale (~ 0.2 ms), suggesting a dominant impulsedriven interaction mode. The observed deceleration of the fragment from 460 m s⁻¹ to 220 m s⁻¹ indicates significant energy transfer into the composite structure. This energy is not dissipated uniformly; instead, it is partitioned across multiple damage mechanisms, including concrete crushing, CFRP delamination, and interfacial debonding.

(3) Under combined blast and fragment loading, damage modes become substantially more complex compared to blast-only scenarios. In the blast-only case, deformation is largely confined to the central region, consistent with pressure-dominated loading of a quasi-brittle material. However, the addition of high-velocity fragments introduces high-gradient, directional stress states, which activate orthotropic failure in CFRP (fiber fracture, matrix cracking) and interface delamination.

The comparison between Fig. 25 and previous blast-only damage patterns Fig. 10 underscores a fundamental shift from centralized plastic deformation to multi-modal failure involving localized penetration, global deformation, and layer separation. This reflects a hybrid loading path where structural response transitions from wave-dominated to penetration-dominated regimes.

(4) The novel aspect of this work is the application of the coupled FDM-SPH approach to simulate the progressive damage of CFRP materials under blast loading. Unlike prior studies focused on metallic or isotropic materials, our research addresses the challenges of simulating anisotropic, rate-dependent composite failure. Notably, this work provides the first insights into the damage mechanisms of concrete-CFRP structures subjected to combined fragment and blast loading. The findings demonstrate that the CFRP composite substantially enhances the structural performance, improving damage resistance.

Future research will aim to deepen the understanding of failure mechanisms in CFRP-reinforced concrete structures subjected to extreme dynamic loading. A key direction is the refinement of the current simulation framework to capture more complex loading environments and multi-scale interactions. For instance, the application of the developed finite difference-smoothed particle hydrodynamics (FDM-SPH) solver will be extended to simulate underwater explosion scenarios. where fluid-structure interaction (FSI) and near-field cavitation effects play a crucial role in damage initiation and propagation. Another promising avenue is the integration of graph-based deep learning models, such as graph neural networks (GNNs) and temporal graph neural networks (TGNNs), with traditional numerical solvers. These models offer a pathway toward building data-driven surrogate models capable of accelerating the prediction of complex, high-dimensional FSI problems. Specifically, GNNs may be used to learn the spatial dependency of nodal states in a mesh or particle system, while TGNNs can capture the time evolution of dynamic events, enabling reduced-order modeling, real-time screening of blast scenarios, and adaptive refinement of computational domains based on learned features.

CRediT authorship contribution statement

Jian-Yu Chen: Writing – review & editing, Writing – original draft, Validation, Software, Resources. Jidong Zhao: Writing – review & editing, Visualization, Supervision. Ruo-Feng Feng: Visualization, Software, Resources. Rui-Chen Ni: Data curation, Conceptualization. Chong Peng: Writing – review & editing, Validation.

Declaration of competing interest

The authors declare that they have no known competing financial interests or personal relationships that could have appeared to influence the work reported in this paper.

Acknowledgements

The authors acknowledge the financial support provided by the National Natural Science Foundation of China (#12202203 and #52439001), and the Research Grants Council of Hong Kong (through TRS #T22-607/24 N, CRF #C7082-22 G, GRF #16203123, #16212724).

Appendix A. EOSs and constitutive models

The EOSs and constitutive models with regard to the concrete and steel materials are summarized in the following appendix.

A.1. HJC constitutive model

The Holmquist-Johnson-Cook (HJC) constitutive model developed by Holmquist, Johnson, and Cook [41] is well-suited for describing the dynamic behavior of concrete medium subjected to large strains, high strain rates, and high pressures. The normalized equivalent stress is defined as

$$\sigma_y^* = \frac{\sigma_y}{f_c} \tag{A.1}$$

where σ_y is the actual equivalent stress; f_c is the quasi-static uniaxial compressive strength. The specific expression for normalized equivalent stress is

$$\sigma_v^* = [A(1-D) + Bp^{*N}](1 + Cln\dot{\varepsilon}^*)$$
(A.2)

where D is the damage $(0 \le D \le 1.0)$; $p^* = p/f_c$; $\dot{\epsilon}^* = \dot{\epsilon}/\dot{\epsilon}_0$ is the dimensionless strain rate; A, B, C, N are material constants. This HJC constitutive model accumulates damage from both plastic volume strain $\Delta \mu^p$ and equivalent plastic strain $\Delta \epsilon^p$, and is expressed as,

$$D = \sum \frac{\Delta \varepsilon^p + \Delta \mu^p}{\varepsilon_f^p + \mu_f^p} \tag{A.3}$$

$$\varepsilon_p^f + \mu_p^f = D_1 (p^* + T^*)^{D_2}$$
 (A.4)

where D_1 and D_2 are constants; $T^* = T/f_c$, T is the maximum tensile hydrostatic pressure the material can withstand.

The response of the pressure-volume is divided into three regions. The first region is referred to as linear elastic region and occurs at $p \le p_{crush}$.

$$p = K_{elastic} \mu \tag{A.5}$$

where $K_{elastic}$ is the elastic bulk modulus; μ is the standard volumetric strain

The second region is the transition region and occurs at $p_{crush} \leq p \leq p_{lock}$. In this region, the air voids are compressed out of the concrete medium, which produces plastic volumetric strain.

$$p = p_{crush} + K_{tran}(\mu - \mu_{crush})$$
(A.6)

where K_{tran} is the bulk modulus in the transition region. The unloading EOS for the transition region is given by

$$p = p_{crush} + K_{tran}(\mu_{max} - \mu_{crush}) + \left[(1 - F)K_{elastic} + FK_1 \right] (\mu - \mu_{max})$$
(A.7)

where $F = (\mu_{max} - \mu_{crush})/(\mu_{plock} - \mu_{crush})$. μ_{max} is the maximum volumetric strain reached prior to unloading; μ_{plock} is the volumetric strain at p_{lock} ; μ_{crush} is the volumetric strain in a uniaxial stress compression test

The third region defines the relationship for the fully dense material, i.e., all air voids are completely removed from the concrete material.

$$p = K_1 \bar{\mu} + K_2 \bar{\mu}^2 + K_3 \bar{\mu}^3 \tag{A.8}$$

where K_1 , K_2 , and K_3 are material constants. $\bar{\mu} = (\mu - \mu_{lock})/(1 + \mu_{lock})$. μ_{lock} is the locking volumetric strain. The unloading EOS for the fully dense region is given by

$$p = K_1 \bar{\mu}_{max} + K_2 \bar{\mu}_{max}^2 + K_3 \bar{\mu}_{max}^3 + K_1 (\mu - \mu_{max})$$
 (A.9)

The tensile pressure is limited to T(1 - D).

A.2. Elasto-plastic constitutive model

The objective stress rate, i.e., Jaumann rate of the Cauchy stress, that does not depend on the frame of reference is introduced for the

determination of stress tensor [42].

$$\dot{S}^{\alpha\beta} = \dot{S}_{I}^{\alpha\beta} + S^{\alpha\gamma}\dot{w}^{\beta\gamma} + S^{\gamma\beta}\dot{w}^{\alpha\gamma}. \tag{A.10}$$

In the elastic range, the Hooke's law is applied,

$$\dot{S}_{J}^{\alpha\beta} = 2G \left(\dot{\varepsilon}^{\alpha\beta} - \frac{1}{3} \delta^{\alpha\beta} \dot{\varepsilon}^{\gamma\gamma} \right), \tag{A.11}$$

in which G is the shear modulus of metal materials. The components of trial elastic deviatoric stress $S_{\rho}^{\alpha\beta}$ can be determined by substituting Eqs.

$$S_e^{\alpha\beta} = \Delta t \left(2G \left(\dot{\varepsilon}^{\alpha\beta} - \frac{1}{3} \delta^{\alpha\beta} \dot{\varepsilon}^{\gamma\gamma} \right) + S^{\alpha\gamma} \dot{w}^{\beta\gamma} + S^{\gamma\beta} \dot{w}^{\alpha\gamma} \right) + S_{(n)}^{\alpha\beta}, \tag{A.12}$$

where $S_{(v)}^{\alpha\beta}$ is the component of deviatoric stress at n-th time step. Based on the SPH methodology, the discretized forms of the strain rate tensor $\dot{\varepsilon}^{\alpha\beta}$ and spin rate tensor $\dot{w}^{\alpha\beta}$ can be derived as follows,

$$\dot{\varepsilon}_{i}^{\alpha\beta} = \frac{1}{2} \sum_{j=1}^{N} \frac{m_{j}}{\rho_{j}} \left(v_{ji}^{\alpha} \frac{\partial W_{ij}}{\partial x_{i}^{\beta}} + v_{ji}^{\beta} \frac{\partial W_{ij}}{\partial x_{i}^{\alpha}} \right) \tag{A.13}$$

$$\dot{w}_{i}^{\alpha\beta} = \frac{1}{2} \sum_{j=1}^{N} \frac{m_{j}}{\rho_{j}} \left(v_{ji}^{\alpha} \frac{\partial W_{ij}}{\partial x_{i}^{\beta}} - v_{ji}^{\beta} \frac{\partial W_{ij}}{\partial x_{i}^{\alpha}} \right)$$
(A.14)

where $v^a_{ji}=v^a_j-v^a_i$. The stress tensor can be determined based on the second invariant J_2 of the deviatoric part of the elastic trial stress and the yield stress σ_Y ,

$$S^{\alpha\beta} = \begin{cases} S_e^{\alpha\beta}, & \text{if } J_2 \le \sigma_Y^2/3; \\ \sqrt{\frac{\sigma_Y^2}{3J_2}} S_e^{\alpha\beta}, & \text{if } J_2 > \sigma_Y^2/3. \end{cases}$$
 (A.15)

The Johnson-Cook model is a function of von mises tensile flow stress based on strain hardening, strain rate hardening, and thermal softening,

$$\sigma_Y = \left[A + B(\varepsilon_p)^n \right] \left[1 + C \ln \left(\frac{\dot{\varepsilon_p}}{\dot{\varepsilon_0}} \right) \right] \left[1 - (T^*)^k \right], \tag{A.16}$$

 T^* is the dimensionless temperature. A, B, C, k are material constants.

A.3. Grüneisen equation of state

Grüneisen equation is an equation of state that relates the density and pressure of a shock-compressed solid material at a given temperature. Grüneisen EOS used in computational mechanics has the following form,

$$p = \begin{cases} \frac{\rho_0 C_0^2 \mu \left[1 + \left(1 - \frac{\gamma}{2} \right) \mu - \frac{\alpha \mu^2}{2} \right]}{\left[1 - (S_1 - 1) \mu - \frac{S_2 \mu^2}{\mu + 1} - \frac{S_3 \mu^3}{(\mu + 1)^2} \right]^2} + (\gamma + \alpha \mu) E & \mu > 0 \\ \rho_0 C_0^2 \mu + (\gamma + \alpha \mu) E & \mu \le 0 \end{cases}$$
(A.17)

where $\mu = \frac{\rho}{\rho_0} - 1$, ρ_0 is the initial density, E is the current specific internal energy. γ , α , S_1 , S_2 , S_3 and C_0 are constant parameters of material.

Data availability

Data will be made available on request.

References

- [1] López-Puente J, Zaera R, Navarro C. An analytical model for high velocity impacts on thin CFRPs woven laminated plates. Int J Solids Struct 2007;44(9):2837-51.
- Wang W, Zhang D, Lu FY, Wang SC, Tang FJ. Experimental study and numerical simulation of the damage mode of a square reinforced concrete slab under close-in explosion. Eng Fail Anal 2013;27:41-51.

- [3] Yan JB, Liu Y, Xu ZX, Li Z, Huang FL, Experimental and numerical analysis of CFRP strengthened RC columns subjected to close-in blast loading. Int J Impact Eng 2020:146:103720
- Reifarth C, Castedo R, Santos AP, Chiquito M, López LM, Pérez-Caldentey A, et al. Numerical and experimental study of externally reinforced RC slabs using FRPs subjected to close-in blast loads. Int J Impact Eng 2021:156:103939.
- Anas SM, Alam M, Umair M, Experimental and numerical investigations on performance of reinforced concrete slabs under explosive-induced air-blast loading: a state-of-the-art review, In: structures; vol. 31, Elsevier; 2021, p. 428-61.
- Anas SM, Alam M. Comparison of existing empirical equations for blast peak positive overpressure from spherical free air and hemispherical surface bursts. Iran J Sci Technol Trans Civ Eng 2022;46(2):965-84.
- Anas SM, Alam M, Umair M, Air-blast and ground shockwave parameters, shallow underground blasting, on the ground and buried shallow underground blast-resistant shelters: a review. Int J Prot Struct 2022;13(1):99-139.
- Patnaik G, Kaushik A, Singh MJ, Rajput A, Prakash G, Borana L. Damage prediction of underground pipelines subjected to blast loading. Arab J Sci Eng 2022:47(10):13559-78
- Rajput A, Kaushik A, Iqbal MA, Gupta NK. Non-linear FE investigation of subsurface tunnel with GFRP protection against internal blast. Int J Impact Eng 2023-172-104423
- Kumar V, Kartik KV, Iqbal MA. Experimental and numerical investigation of reinforced concrete slabs under blast loading. Eng Struct 2020;206:110125.
- Maazoun A, Matthys S, Atoui O, Belkassem B, Lecompte D. Finite element modelling of RC slabs retrofitted with CFRP strips under blast loading. Eng Struct 2022:252:113597
- Børvik T, Olovsson L, Hanssen AG, Dharmasena KP, Hansson H, Wadley HNG. A discrete particle approach to simulate the combined effect of blast and sand impact loading of steel plates. J Mech Phys Solids 2011;59(5):940-58.
- Zhu F, Zhao JD. Peridynamic modelling of blasting induced rock fractures. J Mech Phys Solids 2021:153:104469.
- Liu MB, Liu GR. Smoothed particle hydrodynamics (SPH): an overview and recent developments. Arch Comput Methods Eng 2010;17:25-76.
- [15] Monaghan JJ. Smoothed particle hydrodynamics. Rep Prog Phys 2005;68(8):1703.
- Lucy LB. A numerical approach to the testing of the fission hypothesis. Astron J 1977:82:1013-24.
- Liu MB, Zhang ZL, Feng DL. A density-adaptive SPH method with kernel gradient correction for modeling explosive welding. Comput Mech 2017;60:513-29.
- Chen JY, Lien FS. Simulations for soil explosion and its effects on structures using SPH method. Int J Impact Eng 2018;112:41-51.
- Chen JY, Peng C, Lien FS, Yee E, Zhao XH. Simulations for the explosion in a water-filled tube including cavitation using the SPH method. Computational Particle Mechanics 2019;6:515-27
- Chen JY, Feng DL, Liu JH, Yu SY, Lu Y. Numerical modeling of the damage mechanism of concrete-soil multilayered medium subjected to underground explosion using the GPU-accelerated SPH. Eng Anal Bound Elem 2023;151:265-74
- Sun PN, Le Touzé D, Oger G, Zhang AM. An accurate SPH volume adaptive scheme for modeling strongly-compressible multiphase flows. Part 1: numerical scheme and validations with basic 1D and 2D benchmarks. J Comput Phys 2021;426:109937.
- [22] Shi HT, Yuan GY, Ni BY, Zhang LW. Quasi-brittle ice breaking mechanisms by highvelocity water jet impacts: an investigation based on PD-SPH coupling model and experiments. J Mech Phys Solids 2024;191:105783.
- Yang CY, Zhu F, Zhao JD. A multi-horizon fully coupled thermo-mechanical peridynamics. J Mech Phys Solids 2024;191:105758.
- [24] Peskin CS. The immersed boundary method. Acta Numer 2002;11:479-517.
- Crespo AJ, Domínguez JM, Rogers BD, Gómez-Gesteira M, Longshaw S, Canelas RJFB, et al. Dualsphysics: open-source parallel CFD solver based on smoothed particle hydrodynamics (SPH). Comput Phys Commun 2015;187:204-16.
- [26] Gharehdash S, Barzegar M, Palymskiy IB, Fomin PA. Blast induced fracture modelling using smoothed particle hydrodynamics. Int J Impact Eng 2020;135:103235.
- Dehnen W, Aly H. Improving convergence in smoothed particle hydrodynamics simulations without pairing instability. Mon Not R Astron Soc 2012;425(2):1068-82.
- Liu MB, Liu GR, Zong Z, Lam KY. Computer simulation of high explosive explosion using smoothed particle hydrodynamics methodology. Computers Fluids 2003;32(3):305–22.
- [29] Rabczuk T, Belytschko T. A three-dimensional large deformation meshfree method for arbitrary evolving cracks. Comput Methods Appl Mech Eng 2007;196(29-30):2777-99.
- Zhang SH, Wu D, Lourenço SDN, Hu XY. A generalized non-hourglass updated Lagrangian formulation for SPH solid dynamics. Comput Methods Appl Mech Eng 2025;440:117948.
- Peng C, Wang S, Wu W, Yu HS, Wang C, Chen JY. LOQUAT: an opensource GPU-accelerated SPH solver for geotechnical modeling. Acta Geotechnica 2019:14:1269-87.
- [32] Chang FK, Chang KY. A progressive damage model for laminated composites containing stress concentrations. J Compos Mater 1987;21(9):834-55.
- Brewer JC, Lagace PA, Quadratic stress criterion for initiation of delamination, J Compos Mater 1988;22(12):1141-55.
- Chen JY, Feng DL, Peng C, Ni RC, Wu YX, Li T, et al. A coupled FD-SPH method for shock-structure interaction and dynamic fracture propagation modeling. Appl Math Model 2024;134:288-306.
- Lu Y, Chen JY, Feng DL, Wang LX, Liu MB. Numerical modeling of hypervelocity impacts on carbon fiber reinforced plastics using a GPU-accelerated SPH model. Comput Mech 2023;72(5):907-26.
- Chen JY, Feng DL, Deng SX, Peng C, Lien FS. GPU-accelerated smoothed particle hvdrodynamics modeling of jet formation and penetration capability of shaped charges. J Fluids Struct 2020;99:103171.

- [37] Francesconi A, Giacomuzzo C, Kibe S, Nagao Y, Higashide M. Effects of high-speed impacts on CFRP plates for space applications. Adv Space Res 2012;50(5): 530_48
- [38] Gargano A, Das R, Mouritz AP. Finite element modelling of the explosive blast response of carbon fibre-polymer laminates. Compos Part B Eng 2019;177:107412.
 [39] Vescovini A, Lomazzi L, Giglio M, Manes A. Damage assessment of CFRP laminate
- [39] Vescovini A, Lomazzi L, Giglio M, Manes A. Damage assessment of CFRP laminate plate subjected to close-range blast loading: Hydrocode methodology validation and case study. Procedia Struct Integr 2022;37:439–46.
- [40] Ni RC, Li JS, Zhang X, Zhou X, Cui XX. An immersed boundary-material point method for shock-structure interaction and dynamic fracture. J Comput Phys 2022;470:111558.
- [41] Johnson GR, Stryk RA, Holmquist TJ, Beissel SR. Numerical algorithms in a lagrangian hydrocode., Tech. rep., ALLIANT TECHSYSTEMS INC HOPKINS MN; 1997.
- [42] Randles PW, Libersky LD. Smoothed particle hydrodynamics: some recent improvements and applications. Comput Methods Appl Mech Eng 1996;139(1–4):375–408.